



## Spectral Shaping of Electro-Optical frequency Combs using Machine Learning Techniques

Pinto, Thyago Monteiro Sá

*Publication date:*  
2022

*Document Version*  
Publisher's PDF, also known as Version of record

[Link back to DTU Orbit](#)

*Citation (APA):*  
Pinto, T. M. S. (2022). *Spectral Shaping of Electro-Optical frequency Combs using Machine Learning Techniques*. Technical University of Denmark.

---

### General rights

Copyright and moral rights for the publications made accessible in the public portal are retained by the authors and/or other copyright owners and it is a condition of accessing publications that users recognise and abide by the legal requirements associated with these rights.

- Users may download and print one copy of any publication from the public portal for the purpose of private study or research.
- You may not further distribute the material or use it for any profit-making activity or commercial gain
- You may freely distribute the URL identifying the publication in the public portal

If you believe that this document breaches copyright please contact us providing details, and we will remove access to the work immediately and investigate your claim.

Doctor of Philosophy  
Doctoral thesis in Photonics Engineering



# Spectral Shaping of Electro-Optical frequency Combs using Machine Learning Techniques

Thyago Monteiro Sá Pinto

Kongens Lyngby, 2022



**Supervisor:** Prof. Dr. Darko Zibar  
**Co-supervisor:** Dr. Uliara C. de Moura

**DTU Electro**  
Department of Electrical and Photonics Engineering  
Technical University of Denmark  
Ørsteds Plads  
Building 343  
2800 Kongens Lyngby, Denmark

# Abstract

---

Electro-Optical frequency combs (EOFC)s are widely applied in areas such as metrology, spectroscopy, light detection and ranging, detection of exoplanets, and optical communications systems. Among their advantages, EOFCs offer high stability in the frequency spacing, coherence in the phases, and the possibility to replace an array of lasers with one single optical source. In contrast, EOFCs require strict control over the power distribution per carrier (or line), constituting an essential parameter for efficient EOFC applications. The EOFC power profile is mainly represented by the flatness which is the difference between the maximum to minimum peak power in a frequency window. In this work, machine learning (ML) algorithms are demonstrated to improve the characteristics of EOFCs in terms of flatness, carrier-to-noise ratio (CNR), and the number of carriers. The laser is driven by optimized bias current and RF driving signal composed of multiple harmonics. The bias current, amplitude, and relative phases of the harmonics in the laser RF driving signal are optimized using inverse system design, reinforcement learning, and gradient-free optimizers such as particle swarm optimization (PSO) and differential evolutionary (DE) algorithms. The methods presented in this work support contributions for developing an optimization benchmark for EOFCs, automation of setups including EOFC combs, and use of harmonic composition to improve flatness in combs. The contributions are demonstrated numerically and experimentally using EOFCs based on GS-lasers, Mach-Zehnder modulators, and silicon ring resonator modulators. The optimization techniques yield to improve performance of state-of-art EOFCs, and the results in this work show how ML techniques support the increase of capabilities applications of EOFCs.



# Resumé

---

Elektro-optiske frekvenskamme (EOFC) anvendes i vid udstrækning inden for områder som metrologi, spektroskopi, lysdetektion og afstandsmåling, detektion af exoplaneter og optiske kommunikationssystemer. Blandt deres fordele tilbyder EOFC'er høj stabilitet i frekvensafstanden, sammenhæng i faserne og muligheden for at erstatte et array af lasere med en enkelt optisk kilde. I modsætning hertil kræver EOFC'er streng kontrol over strømfordelingen pr. transportør (eller linje), hvilket udgør en væsentlig parameter for effektive EOFC-applikationer. EOFC-effektprofilen er hovedsageligt repræsenteret af fladheden, dvs. den maksimale til minimale spidseffektforskel af et vist antal linjer i kammen. I dette arbejde er maskinlæringsalgoritmer (ML) demonstreret for at forbedre egenskaberne af EOFC'er med hensyn til fladhed, carrier-to-noise ratio (CNR) og antallet af carriers. Laseren alene udforskes, når den drives af optimeret forspændingsstrøm og RF-signal sammensat af flere harmoniske. Forspændingsstrømmen, amplituden og de relative faser af harmoniske i RF-laser-drivsignalet er optimeret ved hjælp af invers systemdesign, forstærkningsindlæring og gradientfrie optimeringsværktøjer såsom partikelsværmoptimering (PSO) og differentielle evolutionære (DE) algoritmer. Metoderne præsenteret i dette arbejde understøtter bidrag til udvikling af et optimeringsbenchmark for EOFC'er, automatisering af opsætninger inklusiv EOFC-kamme og brug af harmonisk sammensætning til at forbedre fladheden i kamme. Bidragene demonstreres numerisk og eksperimentelt ved hjælp af EOFC'er baseret på GS-lasere, Mach-Zehnder-modulatorer og silicium-ringresonatormodulatorer. Optimeringsteknikkerne giver mulighed for at forbedre ydeevnen af state-of-art EOFC'er, og resultaterne i dette arbejde viser, hvordan ML-teknikker understøtter udvidelsen af kapacitetsanvendelser af EOFC'er.



# Preface

---

The work presented in this thesis was carried out as part of my Ph.D. project from September 1st, 2019 to August 31st, 2022. The Ph.D. took place at the Department of Electrical and Photonics Engineering at the Technical University of Denmark in Kongens Lyngby, Denmark. The Ph.D. was composed of an external stay at the Fraunhofer Institute for Telecommunications, Heinrich Hertz Institute, HHI, Berlin, Germany.

The Ph.D. project was funded by the European Union's Horizon 2020 research and innovation program under the Marie Skłodowska-Curie grant Wideband Optical Networks (grant agreement No 814276). The Ph.D. was supervised by:

- Darko Zibar (main supervisor), Professor, Department of Electrical and Photonics Engineering, Technical University of Denmark, 2800 Kongens Lyngby, Denmark;
- Uliara C. de Moura (co-supervisor), Optical Engineer, NKT Photonics, Birkerød, 3460, Denmark;
- Antonio Napoli (industrial supervisor), Principal Engineer, Infinera, Munich, Germany.



# Acknowledgements

---

This thesis is dedicated to my mother, Marleide, who supported a considerable part of my education. She was the person who taught me how to read and encouraged me to pursue a university degree. During the years of this Ph.D., she came to forget my name and our history, but I am sure if the Alzheimer could allow just for a moment, the day of my defense would be one of her happiest days. Thanks to her support, I attempt to be the first doctor in my family with this thesis. *Te amo, mãe.*

First, I want to thank my supervisor, Darko Zibar, for giving me the opportunity to be part of the Ph.D. program at DTU and for all the guidance during the last few years.

Thanks to Uiara C. Moura for all the patience and support and for being more than my co-supervisor but also a good friend.

Francesco, I don't have words to describe how grateful I am for you joining this work and for all the guidance during the experiments composing this thesis. I learned a lot during this time. Thank you.

Thanks to the Wideband Optical Network (WON) project for supporting this work and for all the training and collaborations. WON has received funding from the European Union's Horizon 2020 research and innovation programme under the Marie Skłodowska-Curie grant agreement 814276. A special thanks to Antonio Napoli, my industrial supervisor, and Tatiana Kilina, project manager. It was a pleasure to interact with such competent professionals who are part of the consortium.

I want to thank Johannes Fisher, Matheus Sena, and Caio Santos for receiving me at Fraunhofer Institute for Telecommunications (HHI), where I developed my external stay. Having the opportunity to experience Berlin while working at HHI was one of the highlights of the last couple of years.

A huge thank you for the collaborators in this work who are also co-authors in the related publications. Besides some of the names already mentioned, thanks to Marko Krstić, Jasna V. Crnjanski and Dejan M. Gvozdić from the University of Belgrade, and also Erwan Weckenmann and Christophe Peucheret from the University of Rennes. It was a pleasure working with you all.

Thanks to the friendly people at the Machine Learning for Photonics (MLPS) group and the High-Speed Optical Communications (HSOC) group for all the coffee breaks, the talks, and shared moments. For my office colleagues, Neethu, Xiansong, and Xiaoyu, thanks for all the nice talks.

To Júlio César Diniz and Camila Souto, thanks for encouraging me to apply for Ph.D. at DTU and for being the good friends you have been for so many years.

I have a lot of good friends to thank in Denmark, Brazil, Portugal, and spread in some other parts of the world. Thanks for staying along, checking on me, and offering me great moments whenever we could finally see each other.

Doing this Ph.D. was only possible due to the unconditional support of the Monteiro family, who was always there for me. A special thanks to my brother Vinícius, my aunts Zélia and Fátima, and my uncle Amadeus for taking care of my mother and giving me the chance to keep going with the Ph.D.

Thanks to my boyfriend Philip for being supportive and giving me the most beautiful weekends during these busy times of doing a Ph.D. during a pandemic.

# List of publications

---

The following publications have resulted from this Ph.D. project.

## Article in a peer-reviewed journal

- [J1] **T. Pinto**, U. C. De Moura, F. Da Ros, M. Krstić, J. V. Crnjanski, A. Napoli, D. Zibar, “Optimization of frequency combs spectral-flatness using evolutionary algorithm”, *Optics Express*, 29(15), 23447-23460, 2021.

## Article to be submitted to a peer-reviewed journal

- [S1] E. Weckenmann, **T. Pinto**, F. Da Ros, U. C. De Moura, D. Zibar, L. Bramerie, M. Gay, D. Perez-Galacho, L. Deniel, D. Marris-Morini, F. Boeuf, and C. Peucheret, “Generation of electro-optic frequency combs with optimized flatness in a silicon ring resonator modulator”, *Optics Letters*, 2022.

## Contributions to international peer-reviewed conference

- [C1] U. C. De Moura, **T. Pinto**, A. M. Rosa Brusin, A. Carena, A. Napoli, D. Zibar, F. Da Ros, “Online versus Offline Optimization Methods for Raman Amplifier Optimization”, *27th OptoElectronics and Communications Conference, OECC 2022*

x

---

# Abbreviations

---

<b>AWG</b>	Arbitrary Waveform Generator
<b>CNR</b>	Carrier to Noise Ratio
<b>CW</b>	Continuous Wave
<b>DC</b>	Direct current
<b>DDPG</b>	Deep Deterministic Policy Gradient
<b>DE</b>	Differential Evolutionary
<b>DFB</b>	Distributed Feedback Laser
<b>DML</b>	Directly Modulated Laser
<b>EOFC</b>	Electro-Optical Frequency Comb
<b>ELM</b>	Extreme Learning Machine
<b>FFT</b>	Fast Fourier Transform
<b>FSR</b>	Free-Spectral Range
<b>GS</b>	Gain Switching
<b>LIDAR</b>	Light Detection and Ranging
<b>LPF</b>	Low Pass Filter
<b>NLI</b>	Nonlinear Interference
<b>NN</b>	Neural Network
<b>ML</b>	Machine Learning
<b>MLL</b>	Mode-locked Laser
<b>MZM</b>	Mach-Zehnder Modulator
<b>PM</b>	Phase Modulator

<b>PMF</b>	Polarization Maintaining Fiber
<b>PPO</b>	Proximal Policy Optimization
<b>PSO</b>	Particle Swarm Optimization
<b>PZM</b>	Polarization Modulator
<b>RF</b>	Radio Frequency
<b>RL</b>	Reinforcement Learning
<b>RMSE</b>	Root Mean Square Error
<b>RP</b>	Random Projection
<b>RRM</b>	Ring Resonator Modulator
<b>SCH</b>	Separate Confinement Heterostructure
<b>SD</b>	Single Drive
<b>SG</b>	Signal Generator
<b>OFC</b>	Optical Frequency Comb
<b>OFDM</b>	Orthogonal Frequency Division Multiplexing
<b>OSA</b>	Optical Spectral Analyzer
<b>TD3</b>	Twin-Delayed Deep Deterministic Policy Gradient

# Contents

---

<b>Abstract</b>	i
<b>Resumé</b>	iii
<b>Preface</b>	v
<b>Acknowledgements</b>	vii
<b>List of publications</b>	ix
<b>Abbreviations</b>	xi
<b>Contents</b>	xiii
<b>1 Introduction</b>	1
<b>Introduction</b>	1
1.1 Motivation and Outline of Contributions . . . . .	2
1.2 Structure of the Thesis . . . . .	3
<b>2 Fundamentals of Electro-Optical Frequency Combs</b>	5
<b>Fundamentals of Electro-Optical Frequency Combs</b>	5
2.1 General characteristics of EOFCs . . . . .	5
2.2 Gain Switching laser model . . . . .	6
2.3 MZM model . . . . .	8
2.4 Silicon Ring resonator modulator model . . . . .	10
2.5 Common EOFC application challenges . . . . .	11
<b>3 Electro-Optical Frequency Comb Characterization using Inverse System Design</b>	13

<b>Electro-Optical Frequency Comb Characterization using Inverse System Design</b>	<b>13</b>
3.1 Machine Learning Inverse System Design Framework for EOFCs . . . . .	14
3.2 Numerical Characterization of Electro-Optical Frequency Combs through Inverse System Design . . . . .	15
3.2.1 Numerical Setup . . . . .	15
3.2.2 EOFCs Numerical Results . . . . .	16
3.3 Experimental Characterization of Electro-Optical Frequency Combs and Optimization through Inverse System Design . . . . .	19
3.3.1 Experimental Setup . . . . .	19
<b>4 EOFC optimization using Gradient-free optimizers</b>	<b>25</b>
<b>EOFC optimization using Gradient-free optimizers</b>	<b>25</b>
4.1 EOFC Gradient-free Optimization Framework . . . . .	25
4.1.1 Problem formulation . . . . .	25
4.1.2 Particle Swarm Optimization Algorithm for EOFC Optimization	26
4.1.3 Differential Evolution Algorithm for EOFC Optimization . . . . .	27
4.2 DE and PSO flatness numerical optimization for GS-laser-based EOFC	29
4.3 DE flatness experimental optimization for GS-laser-based EOFC . . . . .	32
4.3.1 Setup . . . . .	32
4.3.2 Results . . . . .	34
4.3.2.1 Amplitude optimization: one harmonic . . . . .	34
4.3.2.2 Amplitude optimization: three harmonics . . . . .	35
4.3.2.3 Amplitude and phase optimization: three harmonics . . . . .	36
4.3.2.4 DE convergence analysis . . . . .	36
4.4 Experimental Results GS-laser-MZM based EOFC . . . . .	37
4.4.1 Setup Description . . . . .	37
4.4.2 Results . . . . .	38
4.4.2.1 DML-based EOFC setup and single harmonic driving signal . . . . .	39
4.4.2.2 DML-based EOFC setup and multiple harmonic driving signal . . . . .	40
4.4.2.3 DML-MZM-based EOFC setup and laser single har- monic driving signal . . . . .	40
4.4.2.4 DML-MZM-based EOFC setup and multiple harmonic laser driving signal . . . . .	40
4.5 Silicon Ring Resonator Modulator EOFC DE flatness Optimization . . . . .	41
4.5.1 Numerical Analysis RRM EOFC DE Flatness Optimization . . . . .	41
4.5.2 Experimental Evaluation RRM EOFC DE Flatness Optimization	44
<b>5 Reinforcement Learning for EOFC flatness Optimization</b>	<b>47</b>

---

<b>Reinforcement Learning for EOFC flatness Optimization</b>	<b>47</b>
5.1 Reinforcement Learning EOFC Optimization Framework . . . . .	47
5.1.1 Deep Deterministic Policy Gradient Algorithm for EOFC flatness optimization . . . . .	49
5.1.2 Twin-Delayed Deep Deterministic Policy Gradient Algorithm for EOFC flatness optimization . . . . .	51
5.1.3 Proximal Policy Optimization Algorithm for EOFC flatness optimization . . . . .	52
5.1.4 Results GS-laser EOFC RL flatness optimization . . . . .	53
5.1.5 Experimental results DML EOFC DDPG flatness optimization	56
<b>6 Conclusion</b>	<b>59</b>
<b>Conclusion</b>	<b>59</b>
6.1 Summary . . . . .	59
6.2 Outlook . . . . .	60
<b>Bibliography</b>	<b>61</b>



# CHAPTER 1

# Introduction

---

The current increase in telecommunications systems data traffic attracted attention to the use of optical frequency combs (OFC) as an alternative for carriers sources in orthogonal frequency division multiplexing (OFDM) and dense wavelength division multiplexing (DWDM), systems [1, 2]. Moreover, OFCs also found solid applications in metrology [3], spectroscopy [4], light detection and ranging (LIDAR) [5] and even support the detection of exoplanets [6]. Those applications led to various techniques for designing OFCs over the years, especially in designing laser cavity configurations. Among those, a high precision OFC synthesizer which also can be used as a ruler to measure optical frequencies is the work of the Nobel Prize in Physics by Hänsch and Hall in 2005 [7, 8].

In general, OFCs are a sequence of optical carriers equidistant in the spectrum or a set of ultrashort pulses at a defined rate in the time domain. The most popular alternatives for the generation of OFCs are mode-locked lasers (MLL) [9], nonlinear interference (NLI) in highly nonlinear fibers [10] and electro-optical frequency combs (EOFC) based on gain-switching (GS) lasers and phase or amplitude modulators [11]. MLLs offer wideband frequency combs [12], but since the repetition rates are based on the laser cavity, the frequency spaces provided are not so flexible [13]. Unlike MLL and NLI-based combs, EOFCs offer high tunability, mutual phase coherence for the comb lines, and high output power. The flexibility is due to the frequency space between comb-lines being dictated by the laser and modulators driving signals composing the EOFC setup.

Essential features of EOFC are the carrier-to-noise ratio (CNR), the comb flatness and the number of carriers. The flatness is the difference between the maximum and the minimum peak powers of the lines inside a frequency window [14]. The increase of comb-lines within a low flatness is usually made by the combination of GS laser and phase modulators (PM) [15] or Mach-Zehnder modulators (MZM) [16] or a variety of these devices [11]. Moreover, another alternative to increase EOFC flatness is the use of harmonic superposition in the laser or modulator driving signal, especially when using evolutionary computation techniques to optimize the driving signals amplitudes and phases [15, 17–20].

Combining harmonics for the comb driving signals increases the degrees of freedom over the setup. Manual fine-tuning for spectral shaping is time-consuming and not always lead to optimal output for many adjustable parameters. Therefore, machine learning (ML) techniques become an asset to compensate for EOFC limitations such

as phase noise and modulation bandwidth, besides providing setup optimization and a benchmark for parameter optimization of frequency combs. Techniques such as inverse system design [21], evolutionary computation, and reinforcement learning are explored in this scenario. ML methodologies have been investigated in several points of the optical communication link, from the transmitter to the receiver side. In this work, the goal is to use ML algorithms to design the EOFC generation efficiently.

## 1.1 Motivation and Outline of Contributions

In recent years, ML techniques have gained considerable space in optical communications and supported breakthrough transmission performance, system automation, and compensation of physical effects. EOFCs can benefit from using ML techniques to overcome present limitations. In this work, a variety of ML techniques are applied to EOFC numerical and experimental setups, and the main contributions can be summarized as follow:

- **Benchmark for automated EOFC optimization:** EOFCs are defined by theoretical models which can be used to target defined features in the comb, particularly flatness and CNR. Models have limitations compared to actual devices (as shown in Chapter 4), and an optimization framework to be implemented directly on the setup is advantageous. The ML framework provides system automation for future flexible systems, saves time demanded to optimize the EOFC, and can outperform human fine-tuning optimization.
- **Approximated accurate models and prediction for EOFC flatness optimization:** Techniques such as inverse system design and reinforcement learning provide approximated models for the trained setups, which accurately represent the EOFC behavior and can be reused in future optimizations.
- **Driving signal shaping to improve the flatness of EOFC based on GS-lasers:** The use of signal composition is shown numerically and experimentally to improve the flatness performance of EOFCs based only on a GS-laser. Combined with ML optimization techniques, the signal shaping produces high-quality combs with targeted features in an automated setup.
- **Enable power and cost-efficient EOFC generation:** By using ML algorithms is possible to design EOFCs with efficient energy-use-consumption with lower driving signals for the laser and modulators included in the setup. The devices are projected to work in optimal operation points with pre-defined characteristics and flexible configuration.

## 1.2 Structure of the Thesis

This thesis is organized as follows.

In chapter 2, the fundamental building blocks of EOFC are explained. The theoretical extended rate equation model for the generation of EOFCs based on GS-lasers is exposed. The laser uses harmonic superposition over the laser driving signal, which is optimized with ML techniques. The MZM model is explained with a focus on the spectral broadening of EOFCs. Additionally, a ring resonator-based EOFC simplified model is described.

Chapter 3 explains the principles of inverse system design for EOFC characterization. It describes the framework for data extraction and training for inverse models and deeps the analysis with a numerical and experimental validation of the inverse system design over EOFCs based on GS-lasers and driving signal harmonic composition.

Chapter 4 discusses the use of gradient-free optimizers for EOFCs based on GS-lasers, MZMs, and silicon ring resonators. Two algorithms are described and utilized for numerical and experimental optimization of comb features. The results show how these techniques lead to spectral shaping and small flatness EOFCs besides the benefits of combining driving signal shaping with gradient-free optimizers.

Chapter 5 proposes using reinforcement learning algorithms for EOFCs optimization. Reinforcement learning combines some elements of the inverse system design and the gradient-free optimizers mentioned in Chapters 3 and 4. It provides the same level of accuracy as gradient-free algorithms with a lower optimization time.

A summary of the work, conclusions, and future perspectives are presented in chapter 6.



## CHAPTER 2

# Fundamentals of Electro-Optical Frequency Combs

---

Among the alternatives to generate frequency combs, a highly tunable, power efficient, and simple alternative is to drive a GS laser by an/or electrical signal  $I(t)$  [22] or use external electro-optical modulators [23,24]. The combination of a GS laser and modulators allows the EOFC frequency space to be adjusted by changing the devices' driving signals' fundamental frequency. Several setups take advantage of this when designing wide broadband EOFCs, mainly combining GS-lasers with PMs [17, 25], MZMs [19, 26], polarization modulators (PZM) [27, 28] or a combination of multiple modulators in sequence or parallel [29–32]. In this work, a GS-laser model, eventually combined with an MZM, is used for the numerical and experimental analysis. The GS model is described in Section 2.2 while the MZM model is detailed in Section 2.3. Additionally, a ring resonator modulator (RRM) EOFC model is explained in Section 2.4.

## 2.1 General characteristics of EOFCs

Generally, EOFCs are characterized by a sequence of optical carriers equally placed in the frequency domain and centered around a carrier frequency  $f_L$ . The frequency space, repetition rate, or the free-spectral range (FSR) between the lines is an important aspect of the EOFC use. For instance, spectroscopy applications usually requires FSR in the order of MHz to 1-2 GHz [4,33,34] while optical communications use from 12.5 to 100 GHz [2,35]. Regardless of the application, the EOFC is defined within a frequency window and contains a defined number of lines  $L$ . The difference between the maximum and minimum peak power among the  $L$  lines in the frequency window is the flatness. The flatness plays a fundamental aspect in the EOFC application since a uniform power distribution can lead to a more equalized performance for the individual lines [2]. Flat combs usually possess less than 3 dB power imbalance among their

lines. Shaped spectral profiles also help broaden the comb with the use of additional modulators [36]. Another important aspect of the EOFC is the CNR which is the difference between the comb peak powers and the noise floor. A low CNR can lead to poor performance applications for the EOFC [37] since the noise tends to interfere with the power of the individual lines. Additionally, the driving signal characteristics of the laser and the modulators should be considered to avoid the high power values necessary to generate the comb with a defined flatness. In Fig. 2.1, a representation of the basic features of EOFC explored in this work is exemplified.

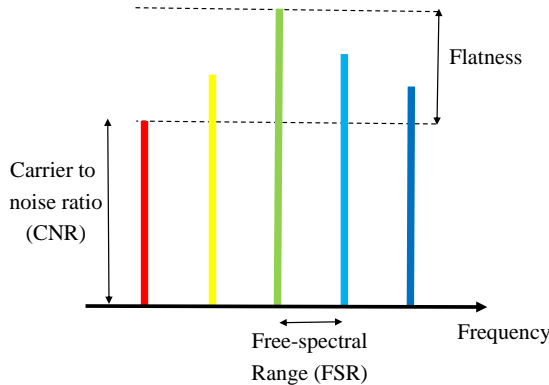


**Figure 2.1.** Basic characteristics of frequency combs.

## 2.2 Gain Switching laser model

The numerical EOFC flatness optimization utilizes a multiple quantum well-distributed feedback laser (DFB) model in GS operation. The laser dynamics are represented by an extended rate equation model [38–40] covering the dynamics of the carrier density in the well regions  $n_w$ , the carrier density in the barrier  $n_b$ , the photon density  $S$ , and the optical phase  $\theta$  as in

$$\frac{dn_b}{dt} = \frac{n_{inj}I}{qV_{tot}} - \frac{n_b}{\tau_b} - \frac{n_b}{\tau_{bw}} + \frac{n_w V_w}{\tau_{wb} V_{tot}}, \quad (2.1)$$

$$\frac{dn_w}{dt} = \frac{n_b V_{tot}}{\tau_{bw} V_w} - \frac{n_w}{\tau_w} - \frac{n_w}{\tau_{wb}} - \frac{v_g \Omega (n_w - n_0) S}{1 + \epsilon S}, \quad (2.2)$$

$$\frac{dS}{dt} = \frac{\Gamma v_g \Omega (n_w - n_0) S}{1 + \epsilon S} - \frac{S}{\tau_p} + \frac{\Gamma R_{sp}}{V_{tot}}, \quad (2.3)$$

$$\frac{d\theta}{dt} = \frac{1}{2} \alpha \Gamma v_g \Omega (n_w - n_{th}), \quad (2.4)$$

where  $V_{tot}$  is the total volume of the separate confinement heterostructure (SCH) and the active region,  $n_{inj}$  is the injection efficiency,  $\epsilon$  is the nonlinear gain suppression coefficient,  $\tau_w$ , and  $\tau_b$  are the carrier lifetimes in the well and in the barrier regions, respectively,  $\tau_{bw}$  represents the capture time,  $\tau_{wb}$  describes the escape time,  $\Omega$  is the differential gain,  $\alpha$  is the linewidth enhancement factor,  $\Gamma$  describes the optical confinement factor,  $V_w$  is the volume of the wells,  $n_0$  is the carrier transparency density,  $R_{sp}$  is the spontaneous emission rate,  $q$  is the electron charge,  $\tau_p$  is the photon lifetime and  $v_g$  represents the group velocity. The model includes carrier transport and parasitic effects. The GS-laser parameters for the numerical evaluation are defined in Table 2.1 based on the characterization of the Gooch & Housego AA0701 series DFB laser used in [18].

**Table 2.1.** Parameters for the laser model of Eq.2.1–2.4.

Parameter	Value
Carrier lifetimes in the well ( $\tau_w$ )	1.5 ns
Carrier lifetimes in the barrier ( $\tau_b$ )	2.5 ns
Carrier transparency density ( $n_0$ )	$4.2 \cdot 10^{18} \text{ cm}^{-3}$
Capture time ( $\tau_{bw}$ )	14.5 ps
Differential gain ( $\Omega$ )	$1.5 \cdot 10^{-15} \text{ cm}^2$
Escape time ( $\tau_{wb}$ )	70 ps
Electron charge ( $q$ )	$1.6 \cdot 10^{-19} \text{ C}$
Group velocity ( $v_g$ )	$8.5 \cdot 10^9 \text{ cm/s}$
Injection efficiency ( $n_{inj}$ )	0.85
Linewidth enhancement factor ( $\alpha$ )	3.5
Nonlinear gain suppression coefficient ( $\epsilon$ )	$2 \cdot 10^{-17} \text{ cm}^4$
Optical confinement factor ( $\Gamma$ )	0.08
Photon lifetime ( $\tau_p$ )	2.3 ps
Spontaneous emission rate ( $R_{sp}$ )	$1.2 \cdot 10^{12} \text{ s}^{-1}$
Total volume of the SCH ( $V_{tot}$ )	$1.03 \cdot 10^{-10} \text{ cm}^3$
Volume of the well ( $V_w$ )	$1.68 \cdot 10^{-11} \text{ cm}^3$

The laser electrical driving signal  $I(t)$  is based on the combination of a bias (direct) current  $c_0$  and a sinusoidal component. If a single harmonic RF signal is used, the sinusoidal function is represented by  $c \sin(2\pi f_0 t)$  where  $c$  is the driving signal amplitude, and  $f_0$  is the fundamental frequency. Driving the laser with  $I(t)$  shifts the laser to above the lasing threshold and generates a sequence of optical pulses equally spaced by  $f_0$ . The modulating or fundamental frequency  $f_0$  defines the EOFC GS-based FSR.

The EOFC characteristics can be improved by using multiple harmonics over the GS-laser driving signal [20]. The combined harmonic driving signal allows more flexibility in shaping  $I(t)$  to achieve EOFC defined profiles. In the case of  $N$  harmonics in  $I(t)$ , the GS-laser driving signal is described by

$$I(t) = c_0 + \sum_{h=1}^N |c_h| \sin(2\pi h f_0 t + \phi_h) \quad (2.5)$$

where  $c_h$  and  $\phi_h$  are the amplitude and phase of the harmonic  $h$  respectively. At the laser output, by solving Eq. 2.1–2.4, the complex electric field  $E_{GS}$  is achieved by [41]

$$E_{GS}(t) = \sqrt{S(t)} \exp\{j\theta(t)\}. \quad (2.6)$$

The EOFC is determined in the frequency domain by applying the Fourier transform over  $E_{GS}(t)$ . An example of the generated EOFC is shown in Fig. 2.1.

## 2.3 MZM model

The MZM is an optical device capable of modulating an input light signal in phase or intensity. The device is based on an electro-optic effect, commonly composed of two PMs in parallel. The MZM is usually employed for spectral broadening of the combs generated by a CW laser. By putting an MZM in sequence with the GS-laser, the output electrical field is defined as

$$E_{MZM} = \frac{1}{2} E_{GS}(t) [\exp\{i\varphi_1\} + \exp\{i\varphi_2\}] \quad (2.7)$$

where  $\varphi_1$  and  $\varphi_2$  are the phases in the PMs of the modulator arms. The phases are expressed as

$$\varphi_j = \frac{\pi}{V_\pi} V_j(t) \text{ for } j = [1 : 2], \quad (2.8)$$

where  $V_j(t)$  is the voltage applied to the  $j$ th PM arm and  $V_\pi$  is the voltage that applied to the PM modulator arm leads to a phase change of  $\pi$  for the input signal. For a multi-harmonic sinusoidal driving signal with  $N$  components,  $V_j(t)$  is defined as

$$V_j(t) = V_{DC_j} + \sum_{h=1}^N |V_{MZM_j}| \sin(2\pi h f_{MZM} t + \phi_{MZM_j}) \text{ for } j = [1 : 2], \quad (2.9)$$

where  $V_{MZM_j}$  is the amplitude and  $\phi_{MZM_j}$  the phase of the signal in the  $j$ th MZM arm, respectively,  $f_{MZM}$  is the modulation frequency of the MZM driving signal and  $V_{DC_j}$  is the bias voltage in the  $j$ th PM arm.  $V_{DC_j}$  defines the MZM operation point, which can be set to operate in a zero, quadrature, or maximum transmission [42]. By applying  $V_j(t)$  and  $\varphi_j$  in Eq. 2.7 for  $j = [1 : 2]$ , the MZM output electrical field is

$$E_{MZM} = E_{GS}(t) \cos\left(\frac{\pi}{2V_\pi}[V_1(t) - V_2(t)]\right) \exp\left(i\frac{\pi}{2V_\pi}[V_1(t) + V_2(t)]\right) \quad (2.10)$$

The MZM possesses two operation modes depending on how the PM arms are driven. A single-drive MZM has the same signal applied to both arms, while a dual-drive MZM has distinct signals driving the PMs in the structure. For the SD-MZM, the signals applied to each arm can have the same amplitude signs and phases or be opposite. When  $V_1(t) = -V_2(t)$ , the MZM is defined as in push-pull configuration, and a pure intensity modulation is achieved. By consequence  $V_{DC_1} = -V_{DC_2}$  and  $V_{MZM_1} = -V_{MZM_2}$ . Therefore, the MZM output electrical in the push-pull configuration field is

$$E_{MZM} = E_{GS}(t) \cos\left(\frac{\pi V_{DC_1}}{V_\pi} + \frac{\pi V_{MZM_1}}{V_\pi} \cos(2\pi f_{MZM} t)\right). \quad (2.11)$$

If we assume  $\zeta = \frac{\pi V_{MZM_1}}{V_\pi}$  and using a Jacobi-Anger expansion over Eq. 2.11,  $E_{MZM}$  can be rewritten as

$$\begin{aligned} E_{MZM} &= E_{GS}(t) \left[ \cos\left(\frac{\pi V_{DC_1}}{V_\pi}\right) \left( J_0(\zeta) + 2 \sum_{k=1}^{\infty} (-1)^k J_{2k}(\zeta) \cos(2k2\pi f_{MZM} t) \right) \right] \\ &- E_{GS}(t) \left[ \sin\left(\frac{\pi V_{DC_1}}{V_\pi}\right) \left( -2 \sum_{k=1}^{\infty} (-1)^k J_{2k-1}(\zeta) \cos((2k-1)2\pi f_{MZM} t) \right) \right], \end{aligned} \quad (2.12)$$

where  $J_k$  is the Bessel function of first kind. The Eq. 2.12 demonstrates that the electrical field produced at the laser output is modulated in intensity by the MZM with harmonics scaled by the Bessel function values. Odd and even harmonics produced by the MZM stage can be totally suppressed by controlling  $V_{DC_1}$  and this us useful for comb expansion. Adjusting the MZM driving signal can place the EOFC generated by the laser symmetrically distributed around the central frequency. The parameters  $\zeta$ ,  $V_{DC_1}$ ,  $V_{MZM_1}$  and  $V_\pi$  have a huge impact over the resulting EOFC spectral profile and are particularly useful for spectral flattening the comb. Therefore, theoretical, numerical and experimental optimization of electro-optical modulators based EOFC usually rely in adjusting the modulators parameters.

The EOFC produced by the GS-laser is preserved while the MZM generates replicas centered in lower or higher frequencies [18]. Meanwhile, the initial phase for the GS-laser-based EOFC is maintained. Consequently, the EOFC flatness can be optimized by distributing the comb lines to maximize the power distribution in a defined frequency window. The lower intensity side-comb lines far from the central frequency can combine with the MZM-produced duplicates and improve the overall comb flatness.

## 2.4 Silicon Ring resonator modulator model

In recent years, integrated EOFCs have gained attention for applications where reduced footprint, cost, and energy consumption are essential, especially in spectroscopy. EOFC generation based on carrier depletion or injection-based have been demonstrated for different structures using PM, MZM and cascaded modulators [43–52]. Among the alternatives, ring-resonator modulators are an attractive technology in terms of power efficiency and compactness, and cascaded RRM or harmonic composition have been investigated to improve the flatness performance of combs generated by these devices.

Ring Resonator modulators are optical cavities structured to couple an optical input field within itself, as presented in Fig. 2.2. The RRM is characterized by a self-coupling field coefficient  $\sigma$ , a cross-coupling coefficient  $\kappa$ , a field attenuation coefficient  $a$ , and a phase shift  $\phi_{RRM}$  in one round-trip inside the device. The field attenuation usually depends on the absorption parameter of the RRM  $\alpha_{RRM}$  while  $\phi_{RRM}$  is a function of the effective index  $n_{eff}$  of the material as in  $\phi_{RRM} = \frac{2\pi L_{RRM}}{\lambda} n_{eff}$  where  $L_{RRM}$  is the ring circumference.

The RRM-based EOFC model analyzed in this work is based on the [53] and the RRM input and output electrical field are represented by the scattering matrix

$$\begin{bmatrix} E_{out} \\ E_{out'} \end{bmatrix} = \begin{bmatrix} \sigma & -i\kappa \\ -i\kappa & \sigma \end{bmatrix} \times \begin{bmatrix} E_{in} \\ E_{in'} \end{bmatrix}. \quad (2.13)$$

Based on Eq. 2.13, the transmission behavior is defined as

$$T = \frac{E_{out}}{E_{in}} = \frac{\sigma - a \exp(-i\phi_{RRM})}{1 - \sigma a \exp(-i\phi_{RRM})}. \quad (2.14)$$

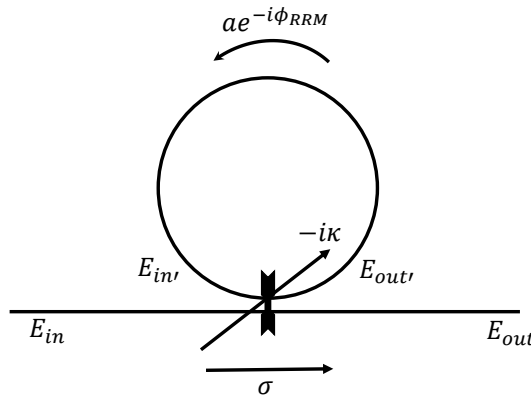


**Figure 2.2.** Schematic representation of a RRM.

The dynamic regime is defined as a Neumann series considering phase and absorption modulations [53, 54]

$$T(t) = \sigma - a(t) \exp(-i\phi_{RRM}(t)) + \sum_{n=1}^{+\infty} \sigma^n [\sigma - a(t - n\tau_r) \exp(-i\phi_{RRM}(t - n\tau_r))] \prod_{m=0}^{n-1} a(t - m\tau_r) \exp(-i\phi_{RRM}(t - m\tau_r)), \quad (2.15)$$

where  $\tau_r$  is the round-trip time for one turn inside the ring.

The EOFC is achieved by calculating the electrical field in the time domain at the output of the Silicon RRM in an all-pass configuration. The RRM uses dopes waveguides based on PN junctions which allow carrier depletion to induce phase shift and variation in the absorption in the silicon material when a voltage-driving signal is applied to the RRM. In essence, the applied voltage signal leads to a variation in the carrier concentrations of electrons  $\Delta N$  and holes  $\Delta P$  for the PN junction waveguides, and those changes impact the refractive index  $\Delta n$  and absorption coefficient  $\Delta\alpha_{RRM}$  in the silica. At  $\lambda = 1550$  nm, the variations are defined by the Soref-Bennet equations [55, 56]

$$\Delta n = -8.8 \times 10^{-22} \Delta N - 8.5 \times 10^{-18} \Delta P^{0.8}, \quad (2.16)$$

$$\Delta\alpha_{RRM} = 8.5 \times 10^{-18} \Delta N + 6.0 \times 10^{-18} \Delta P, \quad (2.17)$$

where  $\Delta N$  and  $\Delta P$  are defined in  $\text{cm}^{-3}$  and  $\Delta\alpha_{RRM}$  in  $\text{cm}^{-1}$ . The solutions of Eq. 2.16 and 2.17 are found using a mode solver and a PN junction simulation [57]. The mode solver enables finding the effective index. At the same time, the absorption is measured based on an absorption reference  $\alpha_0$  when no driving signal is applied as in  $\alpha_{RRM}(V) = \alpha_0 + \Delta\alpha_{RRM}$ .

## 2.5 Common EOFC application challenges

Common challenges for EOFCs are the limited bandwidth of the GS-lasers and modulators available, which limit the number of lines and the EOFC spectral helpful window. Commercial modulators usually have a bandwidth from 25 to 40 GHz [11], but devices with higher bandwidth values can be found [58, 59]. Another concerning point is the noise accumulation resulting from cascaded a laser and several modulators in the EOFC setup, especially considering the lower bandwidth available compared to conventional frequency comb sources. The accumulated noise impacts the GS-laser-based EOFC application, and the overall comb flatness, especially for optical communications applications [60]. Phase noise reduction strategies can be applied to reduce the noise impact [61–63].

Despite the tunability, broadening the EOFC based on modulators may require a high driving signal. Some EOFC require driving signals from 4 to 40 Volts peak-to-peak [16, 23, 64, 65]. High driving signal values can make challenging the comb design in a single chip for commercial purposes [66] although recent progress in integrated EOFC allow flat combs up to 44 lines with FSR between 1 to 12.5 GHz [67–72]. Power-efficient alternatives have been investigated, and machine learning techniques can help accommodate the overall requirements of EOFC for several lines and lower driving signals. Power efficient and wide EOFC can add to their high tunability and make the technology as competitive as MLL and NLI combs.

## CHAPTER 3

# Electro-Optical Frequency Comb Characterization using Inverse System Design

---

The inverse system design is an optimization methodology based on inverting a system relationship input/output and treating the problem from the perspective of output/input. Inverting the mapping input/output allows optimization by targeting defined system behavior or results. Popular alternatives to implement the inverse system design are the genetic algorithm approaches [73, 74] or creating an inverse function or mapping between the output and inputs of a system under analysis [75, 76]. The features to be optimized can be, for example, an optical frequency spectral profile [41, 74, 77, 78], MLL device design [73, 79, 80] or the Raman amplifier gain [21, 81–86] while the inputs correspond to the degrees of freedom of the problem.

The main goal of using the inverse system design for EOFCs is to shape the comb spectrum according to desired features, especially flatness and CNR. The spectral shaping is done by predicting and adjusting the comb input parameters as driving signal amplitudes and relative phases for the devices included in the EOFC setup. The methodology utilizes a multi-layer neural network (NN) to predict and select the input driving signals given a target comb spectral shape. The inverse model can replace solving complex nonlinear equations or extensive device characterization [14, 87, 88]. Additionally, it supports ultra-fast optimization and automation, desirable features for future network autonomous optical systems employing EOFCs [1, 11, 80, 89]. Moreover, offline models based on the inverse system design are a less-computational and time-consuming alternative to gradient-free optimizers [90]. The NN model offers a high degree of flexibility and can be reused for different spectral profiles after trained.

This chapter presents numerical and experimental results for the characterization of EOFCs based on the inverse system design. Differently from the results in [74, 77,

78], the EOFC is based only on the GS-laser, and a numerical evaluation followed by an experimental proof-of-concept is implemented. The comb spectral optimization relies on shaping the laser driving signal using harmonic composition [17, 19, 64, 91, 92]. The inverse model predictions show accurate results with an average RMSE of 0.2 dB for the comb peak powers in the numerical analysis and allow a high degree of programmability for EOFC applications.

### 3.1 Machine Learning Inverse System Design Framework for EOFCs

The EOFC inverse system design corresponds to finding a mapping between the comb features (outputs) and the comb driving signals (inputs). The mapping is represented by a neural network  $\text{NN}_{inv}$  and it is implemented in two stages: (i) data extraction and (ii) model training [93]. For the data extraction when using the EOFC based on the GS-laser only, the input is the vector containing the sampled amplitudes of the three harmonics and the bias current  $\mathbf{I} = [c_0 \ c_1 \ c_2 \ c_3]$  to be applied to the laser as in Eq. 2.5. The output is a vector containing the sampled peak power values of  $L$  EOFC lines around the central frequency  $\mathbf{P} = [P_1 \ P_2 \ \dots \ P_L]$ . For gathering the data, the input is varied, and the output is measured, so the pair input/output is recorded and stored. The values of  $\mathbf{I}$  are uniformly distributed and within the laser limits  $\mathbf{I}^i \sim [\mathcal{U}(c_0^{min}, c_0^{max}), \mathcal{U}(c_1^{min}, c_1^{max}), \mathcal{U}(c_2^{min}, c_2^{max}), \mathcal{U}(c_3^{min}, c_3^{max})]$ . The function  $\mathcal{U}(\cdot)$  represents a random value between the parameters range. It is important for the training data to be uniformly distributed so the  $\text{NN}_{inv}$  can have enough information about the EOFC behavior and provide good generalization properties. In general, the  $\text{NN}_{inv}$  does not accurately extrapolate information outside the training limits. The data-set is represented by  $\mathcal{D}^{M \times (N+L)} = \{([c_0^i, c_1^i, c_2^i, c_3^i], [P_1^i, \dots, P_L^i]) | i = 1, \dots, M\}$ . The training data-set generation is detailed in Algorithm 1 [21, 81].

---

**Algorithm 1:** EOFC Training data-set generation for the Inverse System Design.

---

```

Define the driving signals range  $[c_i^{min}, c_i^{max}]$  for  $i = [1 : 4]$ ;
for  $i=1$  to  $M$  do
     $\mathbf{I}^i \sim [\mathcal{U}(c_0^{min}, c_0^{max}), \mathcal{U}(c_1^{min}, c_1^{max}), \mathcal{U}(c_2^{min}, c_2^{max}), \mathcal{U}(c_3^{min}, c_3^{max})]$  ;
    Evaluate EOFC response  $\mathbf{P}^i = f_s(\mathbf{I}^i)$  ;
    Store par  $\mathcal{D}^i = \{([c_0^i, c_1^i, c_2^i, c_3^i], [P_1^i, \dots, P_L^i])\}$ 
end

```

---

The data-set  $\mathcal{D}$  is split in two groups: a subgroup  $\mathcal{D}_1$  with  $N_{train}$  samples is used for model training while another group  $\mathcal{D}_2$  with  $N_{test}$  points is applied for testing  $\text{NN}_{inv}$ . In the training process a multi-layer neural network  $\text{NN}_{inv}$  learns the inverse mapping between  $\mathbf{P}$  and  $\mathbf{I}$  or  $\mathbf{I} = f_s^{-1}(\mathbf{P})$ .  $\text{NN}_{inv}$  is trained using extreme learning

machine (ELM) [94]. The NN hidden node parameters are randomly assigned following a normal distribution with zero mean and standard deviation  $\sigma_{NN}$ . The model training is least-square based with regularization parameter  $\lambda$ . The hyperparameters  $\lambda, \sigma_{NN}$ , the number of hidden layers ( $N_{HL}$ ), number of nodes per layer  $N_{HN}$  and the activation function  $f_{act}$  are fine-tuned by trial and error. They considerably impact the prediction accuracy of  $NN_{inv}$ . The generalization properties of  $NN_{inv}$  improve by training  $N_{NN}$  different inverse models in parallel and averaging the prediction result. The  $N_{NN}$  distinct models are initialized with different random weights.

After training, the  $NN_{inv}$  weights are fixed. The model is used for driving signal estimation  $\mathbf{I}_{pred}$  for the comb spectral profiles in  $\mathcal{D}_2$ , i.e.,  $\mathbf{I}_{pred} = NN_{inv}(\mathbf{P}_{test})$ . The EOFC peak powers  $\mathbf{P}_{test}$  are the data collected for testing. The calculation of  $\mathbf{I}_{pred}$  is ultra-fast (in comparison with gradient-free optimizers) once it only demands multiplications of the input through the NN layers. The model is validated by measuring the root mean square error (RMSE) between  $\mathbf{I}_{pred}$  and the test data  $\mathbf{I}_{test}$  present in  $\mathcal{D}_2$ . The validation methodology for the EOFC inverse system design is summarised in Algorithm 2 [21, 81].

---

**Algorithm 2:** Inverse System Design for Electro Optical Frequency Combs

---

- Evaluate the EOFC system  $M$  times  $\mathbf{P} = f_s(\mathbf{I})$  to generate the data-set
  - $\mathcal{D}^{M \times (N+L)} = \{([c_0^i, c_1^i, c_2^i, c_3^i], [P_1^i, \dots, P_L^i]) | i = 1, \dots, M\};$
  - Split  $\mathcal{D}$  in one subgroup for training  $\mathcal{D}_1$  and another for testing  $\mathcal{D}_2$  ;
  - Train  $NN_{inv}$  using ELM and  $\mathcal{D}_1$  to learn  $\mathbf{I} = f^{-1}(\mathbf{P})$  ;
  - Compute  $\mathbf{I}_{pred} = NN_{inv}(\mathbf{P}_{test})$  with  $\mathbf{P}_{test}$  within  $\mathcal{D}_2$ ;
  - Evaluate the error  $e = RMSE(\mathbf{I}_{pred}, \mathbf{I}_{test})$  with  $\mathbf{I}_{test}$  within  $\mathcal{D}_2$ ;
- 

## 3.2 Numerical Characterization of Electro-Optical Frequency Combs through Inverse System Design

### 3.2.1 Numerical Setup

The numerical setup for the EOFC inverse system design data-set collection is depicted in Fig. 3.1. For the data extraction  $\mathcal{D}^{M \times (N+L)} = \{([c_0^i, c_1^i, c_2^i, c_3^i], [P_1^i, \dots, P_L^i]) | i = 1, \dots, M\}$ ,  $N = 4$ ,  $L = 19$  and  $M = 5000$ . The current amplitudes in  $\mathbf{I}$  are uniformly distributed within the laser limits from 20 to 80 mA. The harmonic composition is considered in the driving current since it allows flatness improvement compared to using only one harmonic and the fixed bias current [20]. The resulting driving current is used as inputs to and extended rate equation model of the GS-laser [38, 39] described in section 2.2. The laser characteristics are detailed in Table 2.1. The spectrum of the complex electric field at the laser output is achieved by a fast Fourier transform (FFT), followed by a logarithm scale and a normalization. The EOFC peak powers

of  $L$  lines are found using a find peaks function over a defined frequency window including the maximum normalized power  $P = 0$  dB. The peak powers are allocated in the vector  $\mathbf{P}$ . The EOFC carriers are equally spaced by a modulation frequency  $f_0 = 5$  GHz.

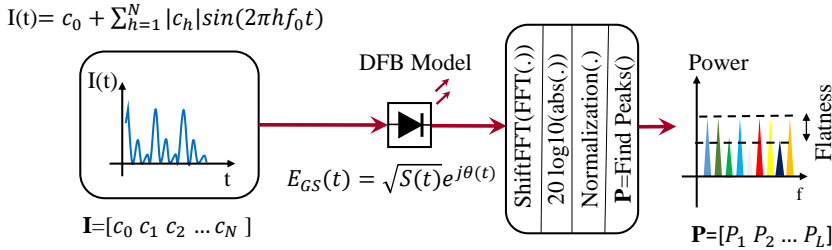


**Figure 3.1.** Numerical setup for EOFC data-set extraction for the inverse system design training and testing.

The data collection follows the Algorithm 1 and the  $NN_{inv}$  model training the procedure in Algorithm 2. The  $NN_{inv}$  fine-tuned hyperparameters are shown in Table 3.1.

**Table 3.1.** Neural network optimized hyperparameters for  $NN_{inv}$  numerical evaluation.

Models	Input signal	$f_{act}$	$N_{HL}$	$N_{HN}$	$N_{NN}$	$\sigma_{NN}$	$\lambda$
$NN_{inv}$	$c_0,$ $c_{1,2,3}$	tanh	2	2000	100	2.5e-2	1e6

### 3.2.2 EOFCs Numerical Results

The  $NN_{inv}$  performance is evaluated by measuring the RMSE between the model predicted input and the real current amplitudes present in the test data  $\mathcal{D}_2$ . The qualitative comparison of the prediction is graphically presented in Fig.3.2 by comparing  $\mathbf{I}_{pred}$  and  $\mathbf{I}_{test}$ . Linear behavior is achieved by showing a good agreement between the predicted values by the inverse model and the collected data. In Figure 3.2, approximately 90% of the RMSE values are distributed within a low error of 0.5 mA. The average RMSE and variance values are presented in Table 3.2 for the four current amplitudes. The  $NN_{inv}$  provides accurate predictions for the test data-set with maximum mean RMSE in the third harmonic of 0.8 mA.

The  $NN_{inv}$  prediction validation performance uses the setup in Fig. 3.3. The  $NN_{inv}$  predicted current amplitudes  $\mathbf{I}_{pred}$  are used to generate a driving signal for the GS-laser model [38,39]. The generated electrical field passes through a shift FFT, logarithm, normalization, and find peaks functions. The EOFC peak powers  $\mathbf{P}_{meas}$

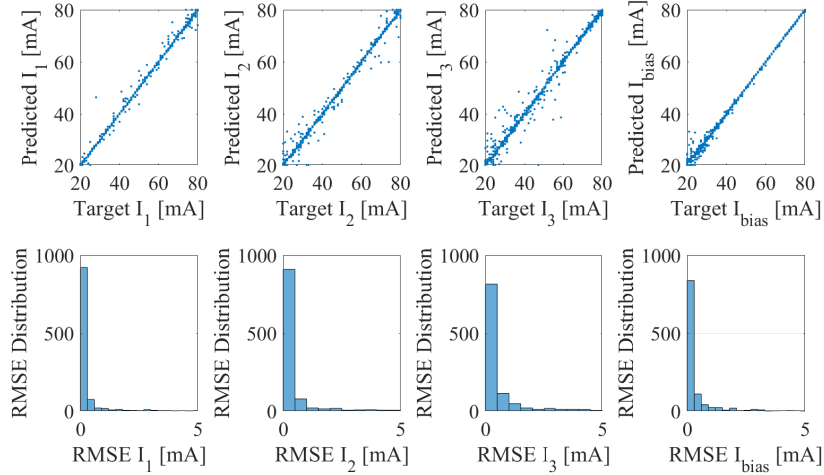


**Figure 3.2.** RMSE  $\text{NN}_{\text{inv}}$  distribution comparison between test and predicted driving currents over 1000 cases of the validation data-set  $\mathcal{D}_2$ .

**Table 3.2.** RMSE comparison between test and predicted driving currents over the validation data-set.

	$c_0$	$c_1$	$c_2$	$c_3$
Mean RMSE [mA]	0.37	0.33	0.53	0.8
RMSE Variance [ $\text{mA}^2$ ]	0.77	2.15	2.08	3.74

by driving the laser with  $\mathbf{I}_{\text{pred}}$  are compared with the arbitrary power values  $\mathbf{P}_{\text{test}}$  in  $\mathcal{D}_2$ . The values  $\mathbf{P}_{\text{test}}$  are known achievable comb profiles.

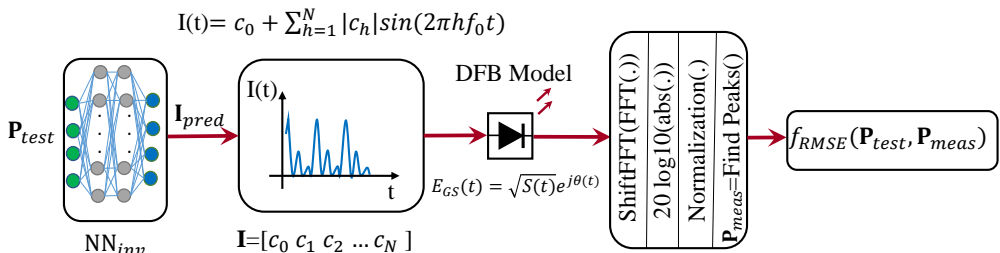


**Figure 3.3.** Numerical validation setup for the EOFC inverse system design.

The RMSE distribution of comparing  $\mathbf{P}_{\text{meas}}$  and  $\mathbf{P}_{\text{test}}$  is shown in Fig. 3.4 for the channels 5 to 13. A significant percentage of the RMSE errors fall within 0.5 dB showing the inverse model accuracy in predicting the EOFC inverse mapping. The

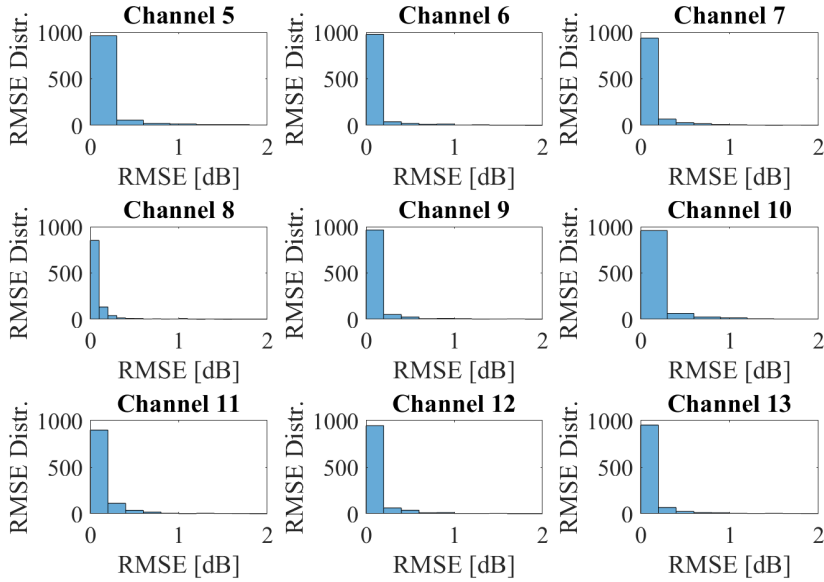


**Figure 3.4.** RMSE distribution comparison between test and predicted peak powers over the numerical validation data-set.

**Table 3.3.** RMSE comparison between test and predicted EOFC peak powers over the numerical test data-set.

Channel	1	2	3	4	5	6	7	8	9	10
Mean RMSE [dB]	0.32	0.28	0.25	0.28	0.24	0.17	0.17	0.11	0.15	0.20
<hr/>										
Channel	11	12	13	14	15	16	17	18	19	-
Mean RMSE [dB]	0.19	0.17	0.13	0.13	0.14	0.16	0.18	0.20	0.22	-

prediction linear behavior can be observed in Fig. 3.5 by the comparison between the predicted EOFC peak power and the test data. The average RMSE for the power estimates in 19 lines around the central frequency is close to 0.5 dB. The framework validation allows the model verification for profiles not used in the model training stage and accuracy for the model predictions.

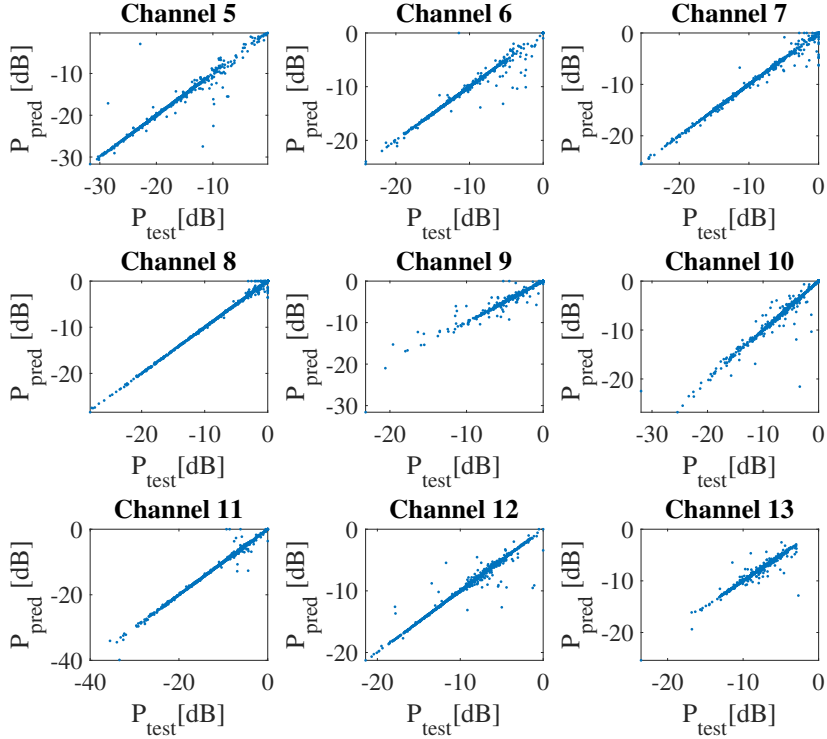


**Figure 3.5.** Comparison between measured and predicted EOFC peak power over the numerical validation data-set using inverse system design.

### 3.3 Experimental Characterization of Electro-Optical Frequency Combs and Optimization through Inverse System Design

#### 3.3.1 Experimental Setup

The experimental setup for EOFC training and test data acquisition for the inverse system design is shown in Fig. 3.6. An evaluation is performed for the cases for the single harmonic ( $N = 1$ ) and three harmonics ( $N = 3$ ) in the laser driving signals. When shaping the driving signal, the signal generators (SGs) Anritsu MG3694C, Agilent E8267D, and Agilent E8247C generate the sinusoidal signal with 5 GHz, 10

GHz, and 15 GHz, respectively. The SG outputs are combined using two couplers with 6 dB loss each. For  $N = 3$ , the SGs clocks are synchronized. The resulting RF signal drives a directly-modulated laser (DML) (NLK1551SSC), while an Agilent E3646A power supply provides the bias current. The laser temperature is controlled by the ThorLabs TED 200 with a resistance set to 10 k $\Omega$ . The EOFC spectrum is measured using a high-resolution optical spectrum analyzer (OSA) Finisar WaveAnalyzer 1500s. The EOFC spectrum profile is saved in the same computer which controls the SGs and power supply output.

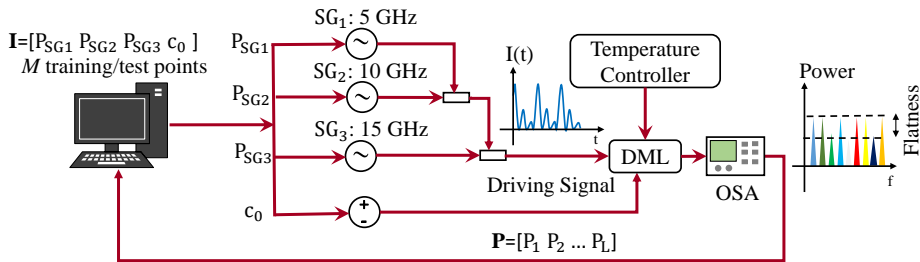


**Figure 3.6.** Experimental setup to capture the data-set for the NN training and test validations.  $c_0$ : Bias current [mA]. SG: Signal Generator.  $P_{sg}$ : Power Signal Generator [dBm]. OSA: Optical Spectrum Analyzer.

In the case of multiple harmonics DML driving signal, the input is the vector containing the bias currents and the electrical power amplitude  $P_{SG}$  at the SG outputs ( $\mathbf{I} = [c_0 \ P_{SG1} \ P_{SG2} \ P_{SG3}]$ ).  $P_{SG1}$ ,  $P_{SG2}$  and  $P_{SG3}$  are the power in dBm at the SG outputs for the first, second and third harmonic, respectively. The resulting  $\mathcal{D}^{M \times (N+L)} = \{(c_0^i, P_{SG1}^i, P_{SG2}^i, P_{SG3}^i, [P_1^i, \dots, P_L^i]) | i = 1, \dots, M\}$  has  $N = 4$  and  $L = 8$ .  $M = 5000$  points are generated and applied to the DML in sequence. The launched power for each harmonic is uniformly distributed within the limits of Table 3.4. The power limits consider the signal after the couplers at the laser input.  $\mathcal{D}$  is split into two parts: 4000 points for training and 1000 for final validation.

**Table 3.4.** DML driving signals limits for the experimental data-set extraction.

	$N = 1$		$N = 3$			
	$c_0$ [mA]	$P_{SG1}$ [dBm]	$c_0$ [mA]	$P_{SG1}$ [dBm]	$P_{SG2}$ [dBm]	$P_{SG3}$ [dBm]
Min	25	-5	35	-5	-5	-5
Max	100	12	100	9	7	5

For  $N = 1$ , the SGs launched power is generated by uniformly distributing values from -5 dBm to 12 dBm. The resulting  $\mathcal{D}^{M \times (N+L)} = \{(c_0^i, P_{SG1}^i, [P_1^i, \dots, P_L^i]) | i = 1, \dots, M\}$  has  $M = 10000$ ,  $N = 1$  and  $L = 5$ .  $\mathcal{D}$  is split into two parts: 7000 points for training and 3000 for testing.

In single and multi-harmonic driving signal cases, the DML is driven by the generated points, and the resulting EOFC spectrum is captured by the OSA. The peak powers  $\mathbf{P}$  of  $L$  carriers in a fixed spectral window are measured using a find peaks function. The data-set  $\mathcal{D}$  is generated following the procedure described in section 3.1 and shown in Algorithm 1.

During the training stage, a multi-layer NN  $\text{NN}_{inv}$  learns the inverse mapping between  $\mathbf{P}$  and  $\mathbf{I}$ . The hyperparameters  $\lambda$ ,  $\sigma_{NN}$ ,  $N_{HL}$ ,  $N_{HN}$  and  $f_{act}$  are optimized and fine-tuned by trial and error in order to minimize the average RMSE between prediction and test data. The generalization properties are improved by averaging the predictions of  $\text{NN}_{inv}$  models. The  $N_{NN}$  are initialized with different random weights. The optimized hyperparameters are shown in Table 3.5. The models require different hyperparameters since the EOFC system relations input/output are distinct for the cases analyzed.

The accuracy of the experimental  $\text{NN}_{inv}$  to predict arbitrary EOFC spectral profiles is evaluated in two ways: applying the  $\text{NN}_{inv}$  predicted driving signals  $\mathbf{I}_{pred}$  to the DML laser or to a NN forward model representing the laser  $\text{NN}_{fw}$ . The validation setup is depicted in Figure 3.7. Since  $N=1$  represents a simpler optimization problem with only two degrees of freedom, validating the inverse system design over the forward model also allows an accurate DML approximated model to be available to data analysis how it will be shown in Chapter 5.

The  $\text{NN}_{fw}$  is used for the single harmonic laser driving signal.  $\mathbf{P}_{test}$  is used as input to  $\text{NN}_{inv}$  and the predicted values  $\mathbf{I}_{pred}$  are subsequently applied to  $\text{NN}_{fw}$ . The hyperparameters for  $\text{NN}_{fw}$  are fine-tuned to minimize the RMSE as before and the optimized values are shown in Table 3.5.  $\text{NN}_{fw}$  represents with low error the DML behavior. The EOFC peak powers  $\mathbf{P}_{meas}$  predicted by  $\text{NN}_{fw}$  are compared with  $\mathbf{P}_{test}$  based on the RMSE. The RMSE distribution is explicit in Fig. 3.8a and Fig. 3.8b. The inverse mapping achieves low RMSE distribution with averages of 1.6 mA and 0.15 dB values when predicting the bias current and RF driving signal amplitude, respectively. Moreover, when applied to the forward model, the system achieves a good degree of accuracy in predicting the EOFC peak powers with RMSE around 0.3 dB/ channel. Important to mention the system validation with a forward model is impacted by error propagation of the cascaded NNs which could decrease the overall framework accuracy.

In the multi-harmonic driving signal scenario, the  $\mathbf{I}_{pred}$  results of applying  $\mathbf{P}_{test}$

**Table 3.5.** NN optimized hyperparameters for the different inverse models based on the EOFC experimental data.

Models	Output signal	$f_{act}$	$N_{HL}$	$N_{HN}$	$N_{NN}$	$\sigma_{NN}$	$\lambda$
$\text{NN}_{inv}$	$c_0, P_{SG1:3}$	tanh	3	800	100	$5.5 \times 10^{-2}$	$10^6$
$\text{NN}_{inv}$	$c_0, P_{SG1}$	tanh	4	800	100	$2.5 \times 10^{-2}$	$10^8$
$\text{NN}_{fw}$	$\mathbf{P}$	tanh	2	800	100	$9.5 \times 10^{-1}$	$10^6$

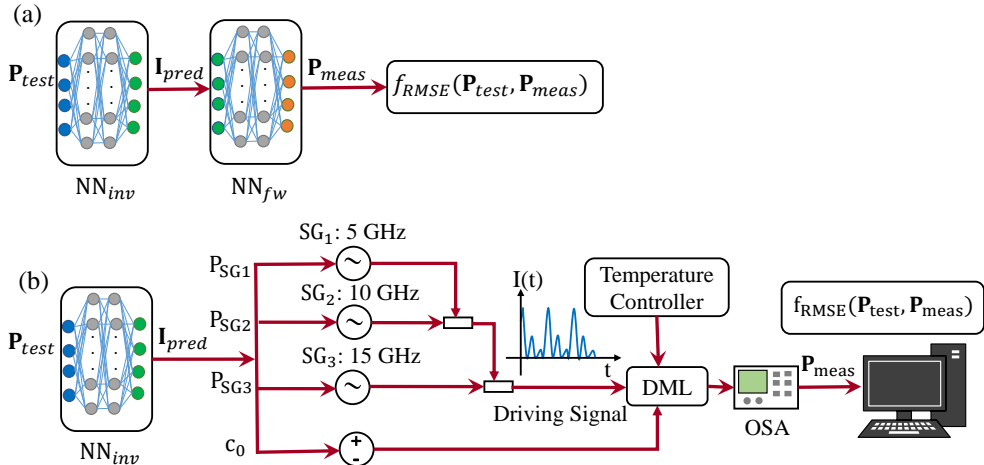


**Figure 3.7.** Experimental setup for evaluation of the inverse system design framework (a) case for one harmonic driving signal (b) case for three harmonics driving signals.

on  $NN_{inv}$  are used to set the values for the SGs and power supply driving the DML as in Fig. 3.7. In sequence, the measured EOFC peak power values  $\mathbf{P}_{meas}$  generated by the laser are compared with  $\mathbf{P}_{test}$ . Accurate prediction performance is obtained using  $NN_{inv}$  to predict the driving signals' amplitudes. The bias current shows an average RMSE of 1.7 mA, while the SGs average RMSE powers are 0.24 dB, 0.36 dB, and 0.59 dB for the first, second, and third harmonic, respectively. The RMSE average distribution for  $N=3$  can be seen in Fig. 3.8c. When comparing the  $\mathbf{P}_{meas}$  and  $\mathbf{P}_{test}$ , the prediction keeps the linear behavior with average RMSE of around 0.31 dB in certain channels. The error distribution is presented in Figure 3.8d. Channel number four presents a higher error for conventionally been the maximum power (0 dB) and wrong prediction usually associated with the power of its sidelines incur in the higher error than the sides comb lines.

The  $NN_{inv}$  do not correspond to the exact inverse mapping for the EOFC but an approximation or a characterization of the EOFC setup. Therefore the model predictions may lead to different values than the EOFC mapping, as usually is the case. The ability to find an accurate inverse model is highly dependent on the quality of the training data. For instance, power spectral profiles with less occurrence in the data-set may be harder to predict as the data-set supports the learning basis for the model. Multiple-to-one mapping is another challenge for training the inverse model, as many spectral profiles can derive from the same driving signal. For this reason, the phases present in the solution of Eq. 2.5 are not considered in the inverse system design methodology. The data-set including varying relative phases leads to high error current predictions for the inverse mapping, and only the amplitudes are considered for the analysis. A strategy to incorporate the phases in shaping the comb driving signal and improve the resulting flatness is the use of gradient-free optimizers

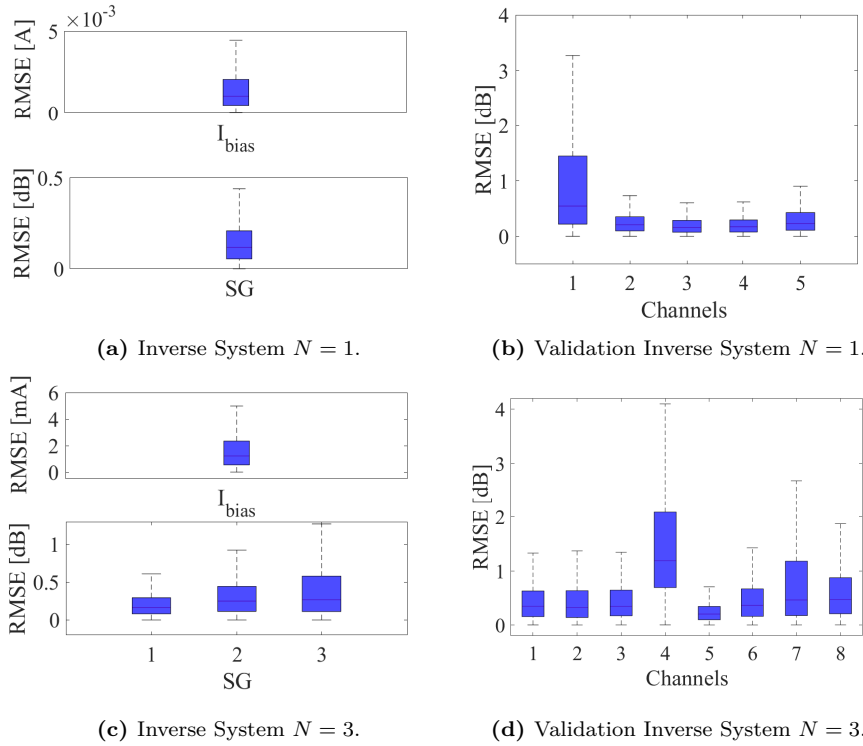


**Figure 3.8.** Experimental RMSE distribution comparison between test and predicted performance over the validation data-set for (a)  $c_0$  and  $P_{SG1}$ , (b) EOFC peak powers  $\mathbf{P}_L$ , (c)  $c_0$  and  $P_{SG1}$ ,  $P_{SG2}$  and  $P_{SG3}$  and (d) EOFC peak powers  $\mathbf{P}_L$ .

as it is presented in Chapter 4.

## Summary of the Chapter

This Chapter discusses the use of inverse system design for spectral prediction and characterization of EOFCs. The numerical and experimental evaluation show the inverse model allows accurate mapping between the spectral profile and the comb driving signals when these are composed of multiple harmonics. Besides accuracy, the inverse model can be re-used for future optimizations since it saves the learned information about the setup during the training stage. The inverse model supports ultra-fast predictions and automatizing systems, including EOFCs.



# CHAPTER 4

# EOFC optimization using Gradient-free optimizers

---

The EOFC spectral profile depends on the driving signal characteristics of the laser and modulators present in the setup [14]. In the case of a GS-laser-MZM-based EOFC, the driving signal features are the amplitudes and the phases of the harmonics composing the device's RF driving signals. Manipulating the phases of the harmonics in the EOFC driving signals can lead to flatness improvement [20] while including the phases in the inverse system design is challenging due to multiple-to-one mapping [95]. Conversely, manually fine-tuning the EOFC performance is cumbersome, time-consuming, and can lead to sub-optimal operational points. For this end, gradient-free optimizers are an accurate alternative to EOFC features optimization [96]. In this Chapter, Particle Swarm Optimization [97] and Differential Evolution algorithm [98] are evaluated for EOFC flatness optimization.

## 4.1 EOFC Gradient-free Optimization Framework

### 4.1.1 Problem formulation

The EOFC gradient-free optimization corresponds to improving the comb characteristics by finding optimal values for the comb driving signals. In the case of a GS-laser-MZM-based EOFC, the inputs are the values of  $c_0$ ,  $N$ ,  $c_h$  in Eq. 2.5 and  $V_{MZM}$ ,  $f_{MZM}$  and  $\phi_{MZM}$  in Eq. 2.9. For the multi-harmonic driving signals, the relative phases are also optimized when the phase reference is set in one harmonic. The relative phases between harmonics  $v$  and  $z$  are represented by  $\Delta\phi_{v,z}$ . The optimization focus on the combined improvement performance of the EOFC flatness, the launched power, the number of carriers, and the CNR. In our case, the main priority is flatness optimization with low CNR.

In using DE and PSO for EOFC optimization, a solution candidate is a vector  $\mathbf{x}$  of parameters representing the EOFC driving signal. The solution candidate depends on the setup and the degrees of freedom over the EOFC input signals. For example, when considering a GS-laser-based EOFC,  $N$  harmonics in the laser driving signal, and a phase reference in the  $N$ th harmonic, the solution is determined like

$$\mathbf{x} = [c_0 \ c_1 \ c_2 \dots c_N \ \Delta\phi_{1,N} \ \Delta\phi_{2,N} \ \dots \Delta\phi_{N-1,N}]. \quad (4.1)$$

The DE and PSO optimization routines are guided by a fitness function that determines the EOFC spectrum features to be optimized. The goal for the cases presented here is to minimize the EOFC flatness for a fixed number of lines. The fitness function  $f(\cdot)$  evaluates the spectra produced by each solution candidate  $\mathbf{x}$  when driving the laser and modulators in the comb setup. The optimized driving signal is achieved iteratively while decreasing the overall  $f(\cdot)$  according to the algorithms' routines. The PSO and DE algorithms applied for EOFCs are described in Sections 4.1.2 and 4.1.3, respectively. In the optimization cases,  $f(\cdot)$  is the variance of the EOFC peak powers for  $L$  consecutive carriers as  $\mathbf{P} = [P_1 \ P_2 \ \dots \ P_L]$ .  $\mathbf{P}$  is obtained by driving the comb with  $\mathbf{x}$ . Mathematically,  $f(\cdot)$  is

$$f(\mathbf{x}) = \frac{1}{L-1} \sum_{l=1}^L |P_l - \mu|^2, \quad (4.2)$$

where  $\mu$  is the mean of  $\mathbf{P}$  as  $\mu = \frac{1}{L} \sum_{l=1}^L P_l$ .

The PSO and DE algorithms allow the optimization to be performed online directly on the EOFC setup. They are beneficial for situations when the model is not known, as happens for the laser present in the experimental validation of Section 4.3.

#### 4.1.2 Particle Swarm Optimization Algorithm for EOFC Optimization

The PSO is a bio-inspired algorithm that resembles the behavior of swarms, and it is characterized by  $N_p$  particles moving in a constrained solution space [97]. In the case of EOFCs optimization, the particles are represented by the solution candidates  $\mathbf{x}$  as exemplified in Eq. 4.1. In contrast, the solution space is defined by the limits of each element present in  $\mathbf{x}$ . The maximum and minimum limits  $\mathbf{x}$  components follow the operational limits of the EOFC laser and modulator driving signals or any design constraints. The PSO comprises three stages: particle position, particle velocity, and fitness evaluation. Each instant or iteration  $k$ , the position  $\mathbf{x}_{k,i}$  of a particle  $i$  is updated by adding to the previous particle position  $\mathbf{x}_{k-1,i}$  its current velocity  $\mathbf{v}_{k,i}$  [99]

$$\mathbf{x}_{k,i} = \mathbf{x}_{k-1,i} + \mathbf{v}_{k,i}, \quad (4.3)$$

where  $i = 1, \dots, N_p$  and  $k = 1, \dots, N_{ite}$  for the number of iterations  $N_{ite}$ .

The individual solution position  $\mathbf{x}_{k,i}$  are highly influenced by  $\mathbf{v}_{k,i}$  [100] which considers a contribution from the best individual particle position  $\mathbf{p}_{best,i}$  and the optimal current group solution  $\mathbf{g}_{best}$  as in

$$\begin{aligned}\mathbf{v}_{k,i} = & w \cdot \mathbf{v}_{k-1,i} + c_{a1} \cdot r_{pso1} (\mathbf{p}_{best,i} - \mathbf{x}_{k-1,i}) \\ & + c_{a2} \cdot r_{pso2} \cdot (\mathbf{g}_{best} - \mathbf{x}_{k-1,i}),\end{aligned}\quad (4.4)$$

where  $w$  is the inertia,  $c_{a1}$  and  $c_{a2}$  are the acceleration coefficients. These are generally equal to 1. The parameters  $r_{pso1}$  and  $r_{pso2}$  represent the exploration and exploitation coefficients, respectively, varying between 0 and 1. These algorithms' hyperparameters define the contribution between individual and collective movement over the particle evolution [101]. The hyperparameters are optimized per optimization problem since they impact convergence and algorithm efficiency.

After the new position  $\mathbf{x}_{k,i}$  is calculated, the solution is evaluated regarding the spectral response it generates when driving the EOFC setup with the comb drive signals provided by  $\mathbf{x}_{k,i}$ . The EOFC response is quantified by  $f(\mathbf{x})$  as explicit in Eq. 4.2. The overall optimization goal for the cases presented here is to minimize  $f(\mathbf{x})$  over  $N_{ite}$  iterations and, therefore, to generate a highly flat EOFC spectrum. The PSO EOFC flatness optimization structure is shown in Algorithm 3.

---

**Algorithm 3:** EOFC PSO Pseudo-Code

---

```

Initialize positions  $\mathbf{X}_0$  and velocities  $\mathbf{V}_0$ ;
Find best initial solution  $\mathbf{g}_{best}$  and  $\mathbf{p}_{best,i}$  by  $f(\mathbf{X}_0)$ ;
while  $k$  less than  $N_{ite}$  do
    for  $i=1$  to  $N_p$  particles do
        Calculate  $\mathbf{v}_{k,i}$  with Eq. 4.4;
        Update  $\mathbf{x}_{k,i}$  with Eq. 4.3;
        Check EOFC solutions limits;
        Apply  $\mathbf{x}_{k,i}$  to the EOFC;
        Evaluate the EOFC fitness function  $f(\mathbf{x}_{k,i})$ ;
        if  $f(\mathbf{x}_{k,i}) < f(\mathbf{p}_{best,i})$  then
            |  $\mathbf{p}_{best,i} = \mathbf{x}_{k,i}$ ;
        end
        if  $f(\mathbf{x}_{k,i}) < f(\mathbf{g}_{best})$  then
            |  $\mathbf{g}_{best} = \mathbf{x}_{k,i}$ ;
        end
    end
end
```

---

#### 4.1.3 Differential Evolution Algorithm for EOFC Optimization

The DE algorithm is a population-based, derivative-free, memoryless class of optimization method [102]. The DE is based on genetic algorithm concepts, and the

optimization follows the survival of the fittest approach over  $N_{ite}$  iterations. Every iteration  $k$  has three stages: mutation, crossover, and fitness evaluation. At iteration  $k = 0$ , a population with size  $N_c$  is generated randomly by uniformly distributing the solutions over the searching space. The searching space is limited by the EOFC driving signals' operational limits. The population comprises the solution candidates  $\mathbf{x}$  as exemplified in Eq. 4.1. This initial population is represented by  $\mathbf{X}_{k=0} = \{\mathbf{x}_{0,1}, \mathbf{x}_{0,i}, \dots, \mathbf{x}_{0,N_c}\}$  with  $i = 1, \dots, N_c$ . For  $k \geq 0$ , in the mutation stage, a donor vector  $\mathbf{v}_{k,i}$  is generated by mixing random solutions from the last iterations  $\mathbf{x}_{k-1,1:N_c}$ . The mixing can be performed in several ways [103, 104]. In this work, the donor vector is generated by combining three solutions from the previous iteration as in

$$\mathbf{v}_{k,i} = \mathbf{x}_{k-1,r_1} + F \cdot (\mathbf{x}_{k-1,r_2} - \mathbf{x}_{k-1,r_3}), \quad i = 1, \dots, N_c, \quad (4.5)$$

where  $r_1, r_2$  and  $r_3$  are random solutions indexes  $\in \{1, 2, \dots, N_c\}$ , and  $F$  is a coefficient varying between 0 and 1. At the crossover phase, the trial vector  $\mathbf{u}_{k,i}$  is created by mixing  $\mathbf{v}_{k,i}$  and  $\mathbf{x}_{k-1,i}$  according to

$$u_{k,i,d} = \begin{cases} v_{k,i,d}, & \text{if } r_c \leq p_c, \\ x_{k-1,i,d}, & \text{if } r_c > p_c, \end{cases} \quad (4.6)$$

where the index  $d$  in  $\mathbf{u}_{k,i}$  represents an EOFC driving signal parameter (amplitude or relative phase),  $p_c$  is the probability of crossover and  $r_c$  is a random number within [0:1] generated per element  $d$ . Before driving the EOFC, the boundaries of  $\mathbf{u}_{k,i}$  are checked, and values outside the device's physical limits are clipped to their minimal or maximum values. In the fitness evaluation step, the EOFC spectrum produced by  $\mathbf{u}_{k,i}$  is checked based on Eq. 4.2. If the EOFC performance generated by  $f(\mathbf{u}_{k,i})$  has a better fitness, the solution candidate is updated as in

$$\mathbf{x}_{k,i} = \begin{cases} \mathbf{u}_{k,i}, & \text{if } f(\mathbf{u}_{k,i}) < f(\mathbf{x}_{k-1,i}) \\ \mathbf{x}_{k-1,i}, & \text{otherwise.} \end{cases} \quad (4.7)$$

The optimal solution  $\mathbf{g}_{best}$  is updated whenever a better global fitness function value is achieved according to

$$\mathbf{g}_{best} = \mathbf{u}_{k,i}, \quad \text{if } f(\mathbf{u}_{k,i}) < f(\mathbf{g}_{best}). \quad (4.8)$$

The EOFC DE optimization routine is described in Algorithm 4.

**Algorithm 4:** EOFC DE Pseudo-Code

---

```

Initialize solutions  $\mathbf{X}_0$ ;
Find best initial solution  $\mathbf{g}_{best}$  by  $f(\mathbf{X}_0)$ ;
while  $k$  less than  $N_{ite}$  do
    for  $i=1$  to  $N_c$  do
        Generate  $\mathbf{v}_{k,i}$  with Eq. 4.5;
        Generate  $\mathbf{u}_{k,i}$  with Eq. 4.6;
        Check EOFC solutions limits;
        Apply the solution to the EOFC;
        Evaluate the EOFC flatness by  $f(\mathbf{u}_{k,i})$ ;
        if  $f(\mathbf{u}_{k,i}) < f(\mathbf{x}_{k-1,i})$  then
            |  $\mathbf{x}_{k,i} = \mathbf{u}_{k,i}$ ;
        end
        else
            |  $\mathbf{x}_{k,i} = \mathbf{x}_{k-1,i}$ ;
        end
        if  $f(\mathbf{u}_{k,i}) < f(\mathbf{g}_{best})$  then
            |  $\mathbf{g}_{best} = \mathbf{u}_{k,i}$ ;
        end
    end
end

```

---

## 4.2 DE and PSO flatness numerical optimization for GS-laser-based EOFC

The DE and PSO algorithms are utilized for a numerical flatness optimization of the EOFC generated based on the GS-laser model described in Section 2.2. The GS-laser is represented by Eq. 2.1–2.4 with parameters of Table 2.1. Considering the fitness evaluation of one solution candidate, the numerical setup is depicted in Fig. 4.1. The use of harmonic superposition over the laser driving signal is analyzed by the comparison of one ( $N = 1$ ) or three ( $N = 3$ ) harmonics in Eq. 2.5. The solution candidates of Eq. 4.1 for  $N = 1$  are defined by  $\mathbf{x} = [c_0 \ c_1]$  and encompass the bias current and the amplitude of the first harmonic. Meanwhile, for  $N = 3$ ,  $\mathbf{x} = [c_0 \ c_1 \ c_2 \ c_3 \ \Delta\phi_{1,3} \ \Delta\phi_{2,3}]$ . The solutions searching space is limited as  $c_h$  within [25:80] mA for  $h = 0$  and within [25:80] mA with  $h \in \{1, 2, 3\}$ , while the relative phases  $\Delta\phi_{1,3}$  and  $\Delta\phi_{2,3}$  between 0 and  $2\pi$ . For  $N = 3$ , the phase reference is in the third harmonic. The solution candidates  $\mathbf{x}$  are provided by the DE and PSO algorithms and drive the DFB laser model as shown in Fig. 4.1.

The spectrum of the complex electric field is calculated at the DFB laser output by using a fast Fourier transform (FFT) function. The spectrum is converted to a logarithm scale, normalized, and the vector  $\mathbf{P}$  is extracted by a *finding peak power*

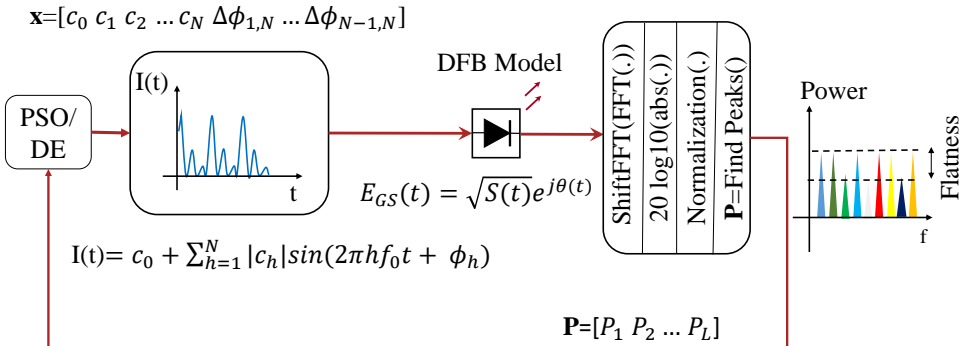


**Figure 4.1.** Numerical setup for EOFC PSO and DE flatness optimization. DE: Differential evolution. PSO: Particle swarm optimization. DFB: Distributed feedback Laser. FFT: Fast Fourier transform.

values function.  $\mathbf{P}$  is centered at the maximum normalized power or 0 dB and contains  $L$  lines. The vector  $\mathbf{P}$  is evaluated by the fitness function of Eq. 4.2 in terms of flatness, and the DE and PSO algorithms perform updates in  $\mathbf{x}_{k,i}$  if appropriate. The process happens for all the  $N_c = N_p$  solutions and  $N_{ite}$  iterations as described in Algorithms 3 and 4.

The DE and PSO hyperparameters are fine-tuned by trial and error and presented in Tables 4.1 and 4.2, respectively. Several EOFC flatness optimization cases were carried out for a different number of lines, and the best compromise flatness/  $L$  was achieved for  $L = 9$ . Additional lines can be obtained when combining the laser with modulators. The fundamental frequency is  $f_0 = 5$  GHz.

The optimized spectral profiles correspond to applying the driving signal  $\mathbf{g}_{best}$  achieved at the end of the DE and PSO optimization routines. The  $\mathbf{g}_{best}$  for the DE and PSO algorithms after  $N_{ite}$  iterations are shown in Table 4.3 for both  $N = 1$  and  $N = 3$ . The algorithms achieve different solution profiles but close values of fitness. Since the algorithms are part of the same class of optimization methodologies, similar performance is expected when considering the equal limitations in the search space.

**Table 4.1.** DE hyperparameters for EOFC optimization.

DE	$N_c$	$F$	$p_c$	$N_{ite}$
Numerical	40	0.6	0.8	100
Experimental	30	0.6	0.8	100

The comparison of single and multiple harmonics in the laser driving signal is also presented in Table 4.3. For  $N = 3$ , a 9-line EOFC with 2.9 dB and 3.3 dB flatness are achieved for the DE and PSO algorithms, respectively. Meanwhile, for  $N = 1$ , the best flatness is 5.7 dB. The harmonic composition combined with the

**Table 4.2.** PSO hyperparameters for EOFC numerical optimization.  $G_1$  and  $G_2$  are random values between 0 and 1 and with  $G_1 + G_2 = 1$ .

PSO	$N_p$	$w$	$r_{psol}$	$r_{psos}$	$N_{ite}$
	40	0.7213	$1.1931 \times G_1$	$1.9331 \times G_1$	100

gradient-free optimizers led to 2.8 dB and 2.4 dB EOFC flatness gain, for the DE and PSO algorithms, respectively, compared with the single harmonic case.

The EOFC flatness optimization is also performed for the setup in Fig. 4.1 but assuming a different FSR of  $f_0 = 9.5$  GHz and the harmonics amplitudes within [20:80] mA. The DE and PSO parameters of Tables 4.1 and 4.2 are maintained. The optimized spectra for  $N = 1$  and  $N = 3$  together with the optimized driving currents and convergence fitness curves are shown in Fig. 4.2. For  $N = 3$ , 9-lines EOFC is achieved with flatness near 2 dB for the PSO and DE algorithms. The combination of harmonic superposition and gradient-free optimizers in a different fundamental frequency led to a flatness improvement compared to the single harmonic alternative. The lower bias current limit led to an EOFC with smaller flatness for all the cases. In these cases, the flatness gain is 1.6 dB for  $N = 3$ . The driving signal features for the optimized EOFC combs are described in Table 4.3 while the currents waveform profiles appear in Fig. 4.2d.

The DE and PSO optimization convergence is shown in Fig. 4.2e. For  $N = 3$ , the fitness value gets close to its final value after 40 and 20 iterations for the 5 GHz and 9.5 GHz cases, respectively. Faster convergence can be achieved depending on the flatness requirements, consequently leading to less computational power and demand for time. The performance continues to improve towards 100 iterations, though slightly.

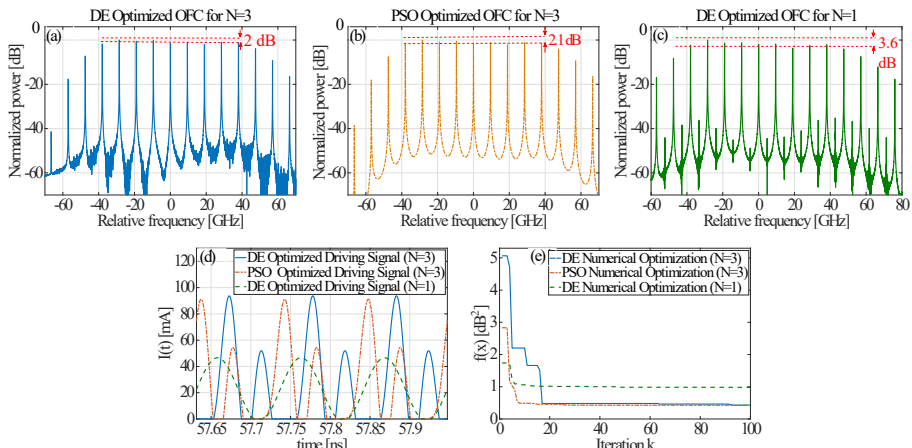


**Figure 4.2.** DE and PSO optimized GS-laser-based EOFCs when considering single ( $N = 1$ ) and multiple harmonics laser driving signal ( $N = 3$ ) and  $f_0 = 9.5$  GHz.

The limitations to obtaining smaller flatness profiles using the model are the laser modulation bandwidth, the number of harmonics in the laser driving signal, and the laser linewidth enhancement factor [18]. The optimization limits the searching space and the possible observable spectra while applying DE and PSO algorithms.

**Table 4.3.** EOFC PSO and DE optimized driving signal components  $\mathbf{x}$  and EOFC performance.

	$\mathbf{x} = [c_0 \ c_1 \ c_2 \ c_3 \ \Delta\phi_{1,3} \ \Delta\phi_{2,3}]$ [mA mA mA mA rad rad]	flatness	$L$
$f_0 = 5 \text{ GHz}$	DE [25.2 20.0 20.0 24.9 5.70 3.56]	2.9	9
	PSO [32.1 29.8 26.4 25.3 0.62 0.76]	3.3	9
	DE [25.0 26.0 - - - - ]	5.7	9
$f_0 = 9.5 \text{ GHz}$	DE [20.1 25.3 35.9 22.9 5.04 3.53]	2.0	9
	PSO [21.3 24.8 33.4 23.9 0.94 1.58]	2.1	9
	DE [22.4 24.2 - - - - ]	3.6	9

## 4.3 DE flatness experimental optimization for GS-laser-based EOFC

### 4.3.1 Setup

A proof-of-concept experimental demo setup of the GS-laser-based EOFC flatness optimization is shown in Fig. 4.3. Since the DE and PSO showed similar performance in the numerical analysis, only the DE is considered in the experimental validation for simplification. The PSO can be used for the same purpose without loss in performance. The DE algorithm generates the solutions  $\mathbf{x}$ , and the individual values are used to set SGs and a power supply. Similar to the numerical analysis, a study comparison between single harmonic ( $N = 1$ ) and three harmonics ( $N = 3$ ) laser driving signal is presented. For  $N = 3$  in Eq. 2.5, a multi-harmonic signal is generated by combining the outputs of the SGs Anritsu MG3694C, Agilent E8267D, and Agilent E8247C with frequencies in 5 GHz, 10 GHz, and 15 GHz, respectively. The SGs outputs are combined using 6 dB loss couplers. The SGs clocks are synchronized. The EOFC is produced by driving a DML (NLK1551SSC) with the SGs combined signal and a bias current generated by an Agilent E3646A power supply. The DML minimum high cutoff frequency is 14 GHz. A ThorLabs TED 200 with a resistance set to 10 k $\Omega$  controls the laser temperature. The DML is not represented by the parameters in Table 2.1, which are fitted to the Gooch & Housego AA0701 series DFB laser used in [18]. The DML output spectrum is measured by a high-resolution OSA Finisar WaveAnalyzer 1500s.

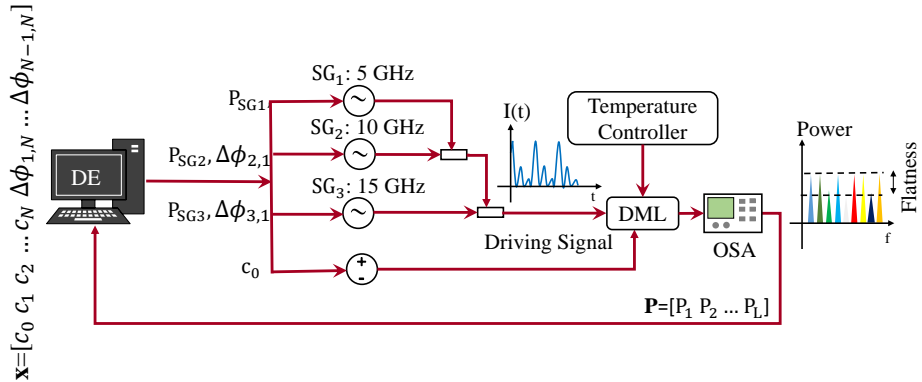


**Figure 4.3.** Experimental setup of EOFC DE flatness optimization. DE: Differential Evolution. SG: Signal Generator.  $c_0$ : Bias current [mA].  $P_{sg}$ : Power Signal Generator [dBm].  $\Delta\phi_{v,z}$ : relative phase for harmonics  $v$  and  $z$ . OSA: Optical Spectrum Analyzer.

The DE EOFC experimental optimization utilizes the parameters of Table 4.1 according to the Algorithm 4 and the fitness function as in Eq. 4.2. The DML maximum bias current and input driving power define the boundaries of the solution. The total RF power is restricted to 12 dBm to avoid damaging the laser. The bias current is limited within [25:120] mA for  $N = 1$  optimization and [35:120] mA for  $N = 3$ . For reference, the laser threshold current is 15 mA. The bias constraints aim to avoid EOFCs spectra with CNR inferior to 20 dB. Since the goal is to allow the optimization for high-quality, low-flatness combs, spectra with CNR below 20 dB are not desirable. The constraint over the CNR is optional. Low CNR EOFC spectra tend to be distorted and noisy and not very useful for comb applications [2]. Additionally, the maximum power in at least one of the EOFC lines is established at -20 dBm, and solutions leading to very low-power EOFCs are excluded during the fitness stage of the DE algorithm.

The DML has a level of amplitude noise which makes the EOFC peak powers  $\mathbf{P}$  vary. The oscillation in  $\mathbf{P}$  impacts the DE optimization since some solutions may show better fitness than previous solutions when in reality, it was mainly an instant variation or transient behavior due to the noise. The EOFC flatness variations are in order of 1 dB. For the DE algorithm to make reasonable decisions when replacing previous solutions, the fitness performance is average over five consecutive measurements. For example, the solution  $\mathbf{x}$  is applied to the DML laser, and five successive measurements of the EOFC spectra are taken. The vector  $\mathbf{P}$  is extracted with the EOFC peak powers for each of the five measurements, and an average is calculated. The averaged peak powers are used for the fitness calculation. Additionally, when a potential new  $\mathbf{g}_{best}$  is found, the candidate is reevaluated for 50 unique consecutive EOFC profile measurements. The  $\mathbf{g}_{best}$  is only replaced by the solution if the fitness

proves to be better than the current  $\mathbf{g}_{best}$ . The averaging during the fitness phase and  $\mathbf{g}_{best}$  reevaluation proved to mitigate the impact of the amplitude noise over the DE flatness optimization. By averaging, a reliable optimization framework is implemented experimentally. The RF driving signal behaviors proved stable and did not significantly impact the optimization.

Several optimization cases were conducted for different values of  $L$  with acceptable flatness around 3 dB. For  $N = 1$ ,  $L = 5$  was the maximum number of lines evaluated. The maximum of  $L = 9$  for  $N = 3$  is considered once eight lines of EOFC result in flatness above 3 dB.

## 4.3.2 Results

### 4.3.2.1 Amplitude optimization: one harmonic

For  $N = 1$  in the driving signal of Eq. 2.5 the EOFC is generated by driving the DML with a sinusoidal signal with a frequency of 5 GHz and the bias current as shown in Fig. 4.4. The RF signal is generated using an SG Anritsu MG3694C. The solution  $\mathbf{x} = [c_0 \ P_{sg1}]$  the DE algorithm uses has  $P_{sg1}$  as the power of the SG. Several optimization cases were carried out considering different values of  $L$ . For  $L = 5$  and  $N_{ite} = 100$ , the optimized solution in presented in Table 4.4 as case 1. The 50 consecutive 1-second intervals measured spectra resulted in an average flatness of 7.1 dB. In comparison, the manual optimization for  $L = 5$  gives a 7.3 dB flatness EOFC when the laser is driven by  $c_0 = 24$  mA and  $P_{sg1} = 10.15$  dBm. The DE and the manual optimization lead to similar results as only two input signals are manipulated. The solutions values are as expected since, for the DML, low EOFC flatness profiles are obtained for high RF power combined with bias current closer to the threshold. A smaller flatness could be obtained for this configuration at the cost of low CNR.

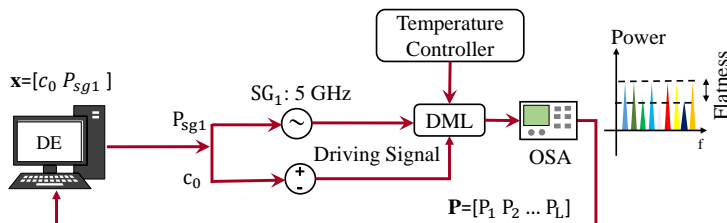


**Figure 4.4.** Experimental setup for EOFC DE flatness optimization. DE: Differential Evolution. SG: Signal Generator.  $c_0$ : Bias current [mA].  $P_{sg}$ : Power Signal Generator [dBm]. OSA: Optical Spectrum Analyzer.

**Table 4.4.** EOFC DE optimized solutions  $\mathbf{x} = [c_0, P_{sg1}, P_{sg2}, P_{sg3}, \Delta\phi_{2,1}, \Delta\phi_{3,1}]$  and comb performances as shown in [20].

Case	$N$	$\mathbf{x}$ [mA, dBm, dBm, dBm, rad, rad]	flatness [dB]	$L$
1	1	[25.0, 12.0, -, -, -, -]	7.1	5
2	3	[39.0, 9.0, 7.4, -5.8, 0, 0]	5.1-7	7
3	3	[48.4, 7.7, 4.5, 4.8, 0, 0]	2.5-3.1	6
4	3	[51.4, 8.8, 4.5, 4.8, 1.9, 2.6]	2-2.3	7
5	3	[40.0, 7.9, 7.4, 1.6, 6.0, 6.3]	6.1	8
6	3	[56.7, 8.5, 7.4, 4.3, 6.1, 3.6]	6.2	9

#### 4.3.2.2 Amplitude optimization: three harmonics

The experimental DE optimization for  $N = 3$  is shown in Fig. 4.3. The searching space for the three harmonics varies according to the ranges in Table 4.5. The values in Table 4.5 represent the maximum and minimum values at the DML input after the couplers. The ranges are different because of the different paths followed by the harmonics in the setup. An electrical amplifier is not considered since it contributes to harmonic distortion and interferes with the optimizer's shaping of the driving signal. Without the amplifier, the harmonic superposition was limited below the maximum operational DML limit of 12 dBm. The DE optimizer has the hyperparameters of Table 4.1 and solutions given by  $\mathbf{x} = [c_0 P_{sg1} P_{sg2} P_{sg3}]$ , where  $P_{sg2}$  and  $P_{sg3}$  are the power of the second and third SGs, respectively.

**Table 4.5.** SGs maximum and minimum values at the DML input.

	SG <sub>1</sub>	SG <sub>2</sub>	SG <sub>3</sub>
Min [dBm]	-5	-5	-5
Max [dBm]	9	7	5

Similarly to the one harmonic case, DE optimization cases for different values of  $L$  were carried out. The best flatness and number of lines combined performance was achieved for  $L = 6$  and corresponded to case 3 in Table 4.4. The DE-optimized solution leads to an averaged flatness of 3 dB, corresponding to the average results from 50 consecutive measurements spaced by a 1-second interval. For  $L = 7$ , a flatness higher than 3 dB is achieved as shown in Table 4.4 as case 2. One main takeaway from the results in Table 4.4 is the improvement over the EOFC flatness brought by using multiple harmonics in the laser driving signal. A 4 dB gain and two extra lines are achieved by adding the second and third harmonic to the laser driving signal and using the DE optimizer to find the best flatness operation point. The driving signal power limitations and the DE restrictions for low CNR are expected to reduce the chances of better EOFC flatness profiles. However, the solution in Table 4.4 also shows the optimized bias current is not close to the laser threshold current, and the CNR does not need to be compromised to improve the EOFC flatness.

### 4.3.2.3 Amplitude and phase optimization: three harmonics

The experimental DE optimization for  $N = 3$  and the relative phases is shown in Fig. 4.3. The solutions candidates are  $\mathbf{x} = [c_0 \ P_{sg1} \ P_{sg2} \ P_{sg3} \ \Delta\phi_{2,1} \ \Delta\phi_{3,1}]$ , with the reference phase in the first harmonic. The best solution to compromise flatness/ $L$  is obtained for  $L = 7$ . The DE-optimized solution leads to a two dB-flatness EOFC for  $L = 7$ . In Table 4.4, the optimized case is presented as case 4. The flatness improvement is due to the flexibility in shaping the laser driving signal performed by the DE optimizer, besides the increase in the searching space. Table 4.4 also shows the optimization solution used for  $L = 8$  (case 5) and  $L = 9$  (case 6), where an EOFC with flatness higher than 3 dB is achieved after the optimization. In comparison, cases 5 and 6 perform better than the single harmonic case with 1 dB flatness gain and a higher number of lines and can be further combined with a modulator for flatness improvement.

### 4.3.2.4 DE convergence analysis

The fitness function of Eq. 4.2 over  $g_{best}$  improves throughout the optimization. The main drawback of DE optimization and gradient-free optimizers is the time demanded. The optimization can not be parallelized in the experimental case since the methodology is applied directly to the setup. By looking at the convergence curves, a performance closer to the final iteration can be achieved after 30 iterations for most cases. This characteristic can speed up the optimization time when faster optimizations are needed. In terms of stability analysis for the setup of Fig. 4.3, the optimal performance was maintained during a 2-hours interval with EOFC flatness.

The DE and PSO gradient-free optimizers allow the optimization to be performed directly on the EOFC setup and have a high degree of flexibility. Unlike the inverse system design, the DE algorithm is not setup-dependent, and distinct EOFC configurations may lead to other optimization points. Moreover, if defined EOFC spectral profile targets are stipulated, the DE needs to run for the individual targets. The evaluation of  $f()$  requests a compromise for the comb spacing, flatness, and the number of optical carriers. The limitations for achieving an EOFC with more lines and better flatness are the limited modulation bandwidth of the GS laser, the laser linewidth enhancement factor, the constraints over the EOFC spectral profiles generated by each solution, and the limitation over the searching space.

The fitness function can be adjusted for specific target spectral profiles. In these cases, the fitness function evaluates the error between the resulting spectrum generated by a solution  $\mathbf{x}$  and the target.

## 4.4 Experimental Results GS-laser-MZM based EOFC

### 4.4.1 Setup Description

The EOFC  $L$ /flatness performance improves by combining the GS-laser with an MZM modulator [11], and the DE optimization can benefit the comb performance by finding low flatness operational points. The experimental setup for GS-laser-MZM-based EOFC DE flatness optimization is shown in Fig. 4.5. An arbitrary waveform generator (AWG) Keysight M8195A generates the RF driving signals for the DML (NLK1551SSC) and the MZM. The AWG sampling frequency is 64 GHz. The DML driving signal is amplified using an electrical amplifier with 20 dB gain, 45 GHz bandwidth, and 15 dBm saturation power. In contrast, the MZM RF signal is amplified using drivers with 22 or 24 dBm saturation power and 26 dB gain. Two cascaded low pass filters minimize the harmonic distortion produced by the electrical amplifiers (LPF)s for both the laser and MZM driving signals. Filters with 3 GHz bandwidth are used for the laser driving signal, while 5 GHz LPFs are for the MZM. For the DML driving signal of Eq. 2.5,  $N = 1$  and  $N = 3$  cases are considered. The fundamental frequency is  $f_0 = 1$  GHz. The single harmonic MZM RF signal of Eq. 2.9 is optimized for  $f_{MZM}$  of 2 or 3 GHz.

The setup uses the same laser and temperature controller in the same operation mode as the setup of Fig. 4.3. The temperature controller remains constant along the optimization routine. The laser output is modulated using a single drive (SD)-MZM Fujitsu FTM7938EZ in push-pull operation mode. An Agilent E3646A power supply provides the laser bias current and the MZM bias voltage. The same OSA measures the EOFC spectrum as in the setup of Fig. 4.3. The DE algorithm optimizes the DML bias current, while the MZM is biased at the maximum operating point of 1.5 V. The MZM  $V_\pi$  is 5.65 V, and the optical bandwidth (-3 dB) is superior to 25 GHz. The EOFC flatness performance is improved by the DE algorithm, which sets the AWG-generated signals waveforms and power supply outputs.

The DE algorithm is characterized by  $N_c = 35$  solution candidates  $\mathbf{x}$ , probability of crossover  $p_c = 0.8$ , scaling factor  $F = 0.6$ , and searching space constrained by the operation limits of the laser and MZM. A different cost function  $f(\cdot)$  from the previous optimization is utilized.  $f(\cdot)$  is the minimum variance of the vector containing the peak power values of  $L+1$  consecutive EOFC carriers as in  $\mathbf{P} = [P_{ii} P_{ii+1} \dots P_{ii+L}]$ , i.e., the region with smallest flatness. The elements  $ii$  vary from 1 to the maximum peak power captured from the EOFC  $N_{ofc} = 24$ .  $\mathbf{P}$  is the vector containing the EOFC peak powers values produced by  $\mathbf{x}$  when applied to the laser and MZM in the setup of Fig. 4.5. The variance is calculated by groups of  $L + 1$  EOFC comb lines in sequence, and the minimum value is chosen. Per group of  $L + 1$  inside  $\mathbf{P}$ , the fitness function is described as

$$f(\mathbf{x}) = \min_{1 \leq ii \leq N_{ofc}-L} \left[ \frac{1}{L-1} \sum_{l=ii}^{ii+L} |P_l - \mu|^2 \right], \quad (4.9)$$

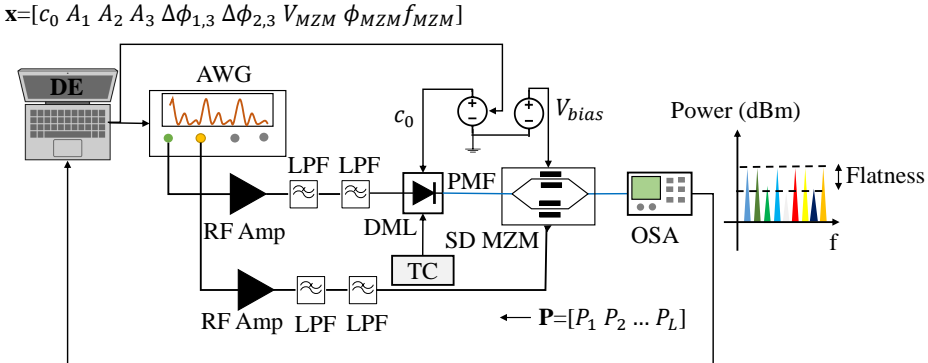


**Figure 4.5.** EOFC experimental setup for EOFC flatness optimization using DE algorithm. AWG: Arbitrary Waveform Generator. LPF: Low Pass Filter. RF: Radio Frequency. SD MZM: Single-Drive Mach-Zehnder Modulator. OSA: Optical Spectral Analyzer. DML: Directly Modulated Laser. TC: Temperature Controller. PM: Polarization Maintaining. DE: Differential Evolution.

where  $\mu$  is the mean of  $\mathbf{P}$  as  $\mu = \frac{1}{L} \sum_{l=1}^L P_l$ .

The total RF power at the laser input is restricted to 12 dBm to avoid damaging the laser. The saturation power of the amplifier limits the maximum RF power driving the MZM at 24 dBm. The laser bias current boundaries are determined beyond its threshold value of 15 mA and the maximum supported current in the interval [35:100] mA. The reason is to avoid solutions leading to an EOFC spectrum with CNR inferior to 20 dB, observable for lower values of bias current as mentioned in Section 4.3.

As mentioned, the DML possesses a level of amplitude noise. The EOFC spectrum generated by each solution  $\mathbf{x}$  is averaged over three consecutive measurements to minimize the impact of these variations over the DE optimization accuracy. The averaging improves the DE optimization and allows the algorithm to mitigate the effects of the amplitude noise. Moreover, potential  $\mathbf{g}_{best}$  are reevaluated in terms of EOFC response with the average of 30 new spectrum captures.  $\mathbf{g}_{best}$  is only replaced if the new best solutions provide better flatness after the re-evaluation. Considering the time demanded for the DE flatness optimization, 30 measurements represent a balanced compromise for replacing  $\mathbf{g}_{best}$ .

#### 4.4.2 Results

The parameter  $L$  is varied between 9 to 15 for the following EOFC setups: (i) laser alone driven by a single harmonic driving signal ( $N = 1$ ), (ii) laser alone driven by a multiple harmonic driving signal ( $N = 3$ ), (iii) laser and MZM combined with single harmonic driving signal for both devices ( $N = 1$ ), (iv) laser and MZM combined with laser multiple harmonic driving signal ( $N = 3$ ) and modulator single harmonic

driving signal. Different combinations were explored in the same setup to provide a fair comparison for the EOFC flatness optimization.

#### 4.4.2.1 DML-based EOFC setup and single harmonic driving signal

The EOFC generation using the DML alone is achieved using the setup in Fig. 4.6. The single harmonic laser driving signal is set at a fundamental frequency of 1 GHz. The signal generated by the AWG is applied directly to the DML. The solution candidates are defined as  $\mathbf{x} = [c_0 \ A_1 \ A_2 \ A_3 \ \Delta\phi_{1,3} \ \Delta\phi_{2,3}]$ , where  $A_1$  is the digital amplitude of the harmonic. After 100 iterations, the DE algorithm finds the optimized solution presented in Table 4.6 as case 1. Driving the laser with these values and measuring 30 spectra with a 1-second interval, the average achieved flatness is 6.3 dB for nine lines, as presented in Fig. 4.7a. The results are slightly improved if, instead of the AWG, the single harmonic driving signal is provided by an SG Rohde & Schwarz SMR40 with launched power  $P_{sg1}$ .

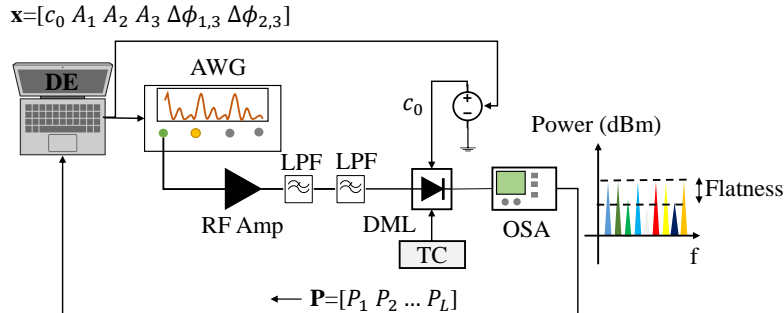


**Figure 4.6.** EOFC experimental setup per solution/iteration for flatness optimization using DE algorithm. AWG: Arbitrary Waveform Generator. LPF: Low Pass Filter. RF: Radio Frequency. OSA: Optical Spectral Analyzer. DML: Directly Modulated Laser. TC: Temperature Controller. DE: Differential Evolution.

**Table 4.6.** DE experimental flatness optimized solutions  $\mathbf{x}$  for a GS-laser-MZM based EOFC.

Case	$N$	$[c_0 \ A_1 \ A_2 \ A_3 \ \Delta\phi_{2,1} \ \Delta\phi_{3,1} \ V_{MZM} \ \phi_{MZM} \ f_{MZM}]$ [mA - - - rad rad - rad GHz]]	Flatness	$L$
1	1	[99.2 0.82 - - - - - ]	6.4	9
2	3	[66.4 1.0 0.2 1.0 0.22 1.84 - - - ]	3.3	11
3	1	[90.1 0.78 - - - 0.93 2.3 2 ]	3.7	13
4	3	[36.4 0.67 0.38 0.10 3.56 3.63 0.9 0 2 ]	1.6	13

#### 4.4.2.2 DML-based EOFC setup and multiple harmonic driving signal

The EOFC generation using the laser alone is achieved using the setup in Fig. 4.6. The AWG generates the multiple harmonic laser driving signal, amplified and filtered before it reaches the DML. The laser input power varies between 4 and 12 dBm. The electrical amplifier contributes to harmonic distortion for the harmonics in 4 and 5 GHz, but the 3 GHz LPF minimizes the effect. The solution candidates are represented by  $\mathbf{x} = [c_0 \ A_1 \ A_2 \ A_3 \ \Delta\phi_{1,3} \ \Delta\phi_{2,3}]$ , where  $A_2$  and  $A_3$  are the digital amplitudes of the second and third harmonics generated by the AWG, respectively,  $\Delta\phi_{1,3}$  and  $\Delta\phi_{2,3}$  are the relative phases in respect to the third harmonic.

Different values for  $L$  in the cost function of Eq. 4.9 are evaluated throughout the DE optimization. The best compromise flatness/ $L$  is obtained for 11 carriers at the solution point presented in Table 4.6 as case 2. The achieved flatness is 3.3 dB, improved by using three harmonics in the laser driving signal. The EOFC obtained in the final solution is depicted in Fig. 4.7b.

#### 4.4.2.3 DML-MZM-based EOFC setup and laser single harmonic driving signal

The EOFC setup based on the DML and MZM is depicted in Fig. 4.5. The solution candidates are expanded by including the MZM driving signal features as in  $\mathbf{x} = [c_0 \ A_1 \ V_{MZM} \ \phi_{MZM} \ f_{MZM}]$ . After the DE optimization for different values of  $L$  in the cost function of Eq. 4.9, the best compromise flatness/ $L$  is obtained for case 3 in Table 4.6. The optimized EOFC is presented in Fig. 4.7c. For 13 comb lines, the EOFC flatness achieved is 3.7 dB, which corresponds with an improvement in comparison with the use of the laser alone and stays comparable with the use of multiple harmonics in the laser driving signal when taking the amplitude noise into account. The power limitation over the MZM driving signal is expected to limit the number of achievable comb lines.

#### 4.4.2.4 DML-MZM-based EOFC setup and multiple harmonic laser driving signal

The EOFC setup based on the DML and MZM is depicted in Fig. 4.5. The solution candidates are represented by  $\mathbf{x} = [c_0 \ A_1 \ A_2 \ A_3 \ \Delta\phi_{1,3} \ \Delta\phi_{2,3} \ V_{MZM} \ \phi_{MZM} \ f_{MZM}]$ . In this case, 13 comb lines with a narrow flatness of 1.6 dB are achieved for the optimized DE EOFC. The overall EOFC spectrum is shown in Fig. 4.7d and the optimized solution in Table 4.6 as case 4. The combined use of multiple harmonics in the laser driving signal and the DE optimization algorithm is proved to improve the flatness characteristics of the resulting EOFC considerably. The flatness optimization of 15 lines did not lead to a narrowed flatness EOFC, and the overall best result is presented for 13 lines. Broadening the EOFC is possible by manipulating the MZM driving signals. As shown in [18], odd or even harmonics can be canceled in the device output electrical field of Eq. 2.12, and properly setting the MZM fundamental frequency can lead to spectral broadening based on replicas of the EOFC produced by the laser in the first stage of the EOFC setup. The combination of a theoretical

approach with gradient-free optimizers or other ML techniques can push forward the performance of EOFC based on GS-lasers and MZMs.

The DE algorithm treats the EOFC input/output relationship as a black box. The experiment serves as a proof of concept for applying the DE algorithm and the benefits of shaping the RF laser driving signals to achieve better flatness in the comb.

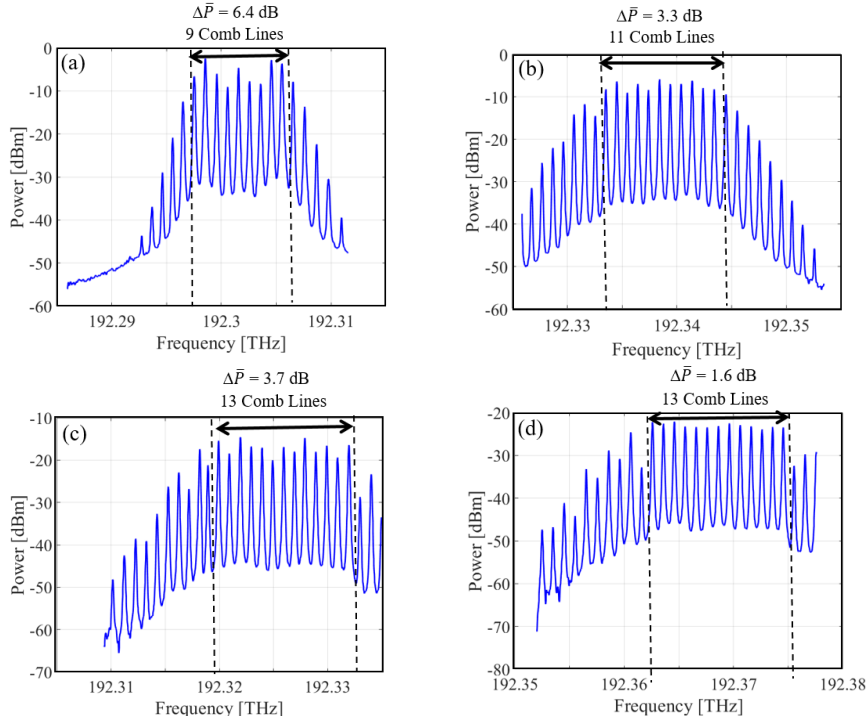


**Figure 4.7.** Experimental EOFC optimized (averaged flatness of 30 measured spectra overlapped) using DE algorithms for: (a) Setup- DML and  $N = 1$ , (b) Setup- DML and  $N = 3$  (c) Setup- DML-MZM and  $N = 1$  and (d) Setup- DML-MZM and  $N = 3$ .

## 4.5 Silicon Ring Resonator Modulator EOFC DE flatness Optimization

### 4.5.1 Numerical Analysis RRM EOFC DE Flatness Optimization

An alternative to generating EOFCs is using RRMs, as shown in Section 2.4. For the numerical flatness evaluation, the RRM model is based on a standard all-pass ring configuration with a carrier-depletion based on a phase-shifter implemented as

a lateral PN junction in the ring waveguide [56]. The RRM has a radius of  $20 \mu\text{m}$ ,  $3 \times 10^4$  of loaded Q-factor, 14.6 dB/cm of intrinsic loss, and 0.975 of self-coupling field coefficient. In a similar approach to the GS-laser EOFC from Section 4.2, the flatness improvement for the RRM EOFC is achieved by combining the harmonic superposition over the device driving signal, and the DE optimization [105, 106]. The multiple harmonics RRM driving signal is described by

$$V(t) = V_{dc} + \sum_{n=1}^{N_h} V_n \sin(2\pi n f_g t + \phi_n), \quad (4.10)$$

where  $V_{dc}$  is the bias voltage,  $V_n$  represents the amplitudes of each harmonic,  $\phi_n$  their phases and  $f_g$  is the fundamental modulation frequency.

The DE optimization is used over the RRM EOFC model following the Algorithm 4. The solution candidates are defined as  $\mathbf{x} = [V_{dc} \ V_1 \ V_2 \ V_3 \ \Delta\phi_{1,3} \ \Delta\phi_{2,3} \ f_g \ \Delta\lambda]$ , where  $\Delta\phi_{1,3}$  and  $\Delta\phi_{2,3}$  represent the relative phases of the first and second harmonic in relation to the third harmonic, respectively, and  $\Delta\lambda$  is the wavelength-detuning value  $\Delta\lambda = \lambda_s - \lambda_0$ . The source wavelength is  $\lambda_s$ , while  $\lambda_0$  is the wavelength in the absence of applied voltage. The DE fitness function is the one in Eq. 4.2, and the optimization goal is to minimize the EOFC flatness throughout the iterations. The solutions elements within  $\mathbf{x}$  were limited to the range specified in Table 4.7.

**Table 4.7.** RMM maximum and minimum driving signal values.

	$V_{dc} + V_1 + V_2 + V_3$ [V]	$\Delta\lambda$ [pm]	$f_g$ [GHz]
Min	-14	-200	1
Max	0	200	10

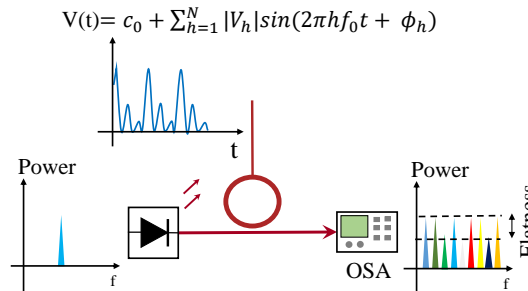


**Figure 4.8.** RRM setup of the online flatness optimization using DE Algorithm.  $f_g$ : optical carrier frequency.  $f_g$ : fundamental modulation frequency.  $\delta$ : flatness. CW: continuous wave, OSA: optical spectrum analyzer.

Several DE optimization cases were carried out for a different number of EOFC lines  $L$  produced by the RRM model. The parameter  $L$  is fixed per optimization case. The best compromise flatness/ $L$  was observed for  $L = 7$  and an EOFC flatness of 1.5 dB, as presented in Fig. 4.9. The  $\mathbf{g}_{best}$  is shown in Table 4.8 for the simulated case and the driving signal waveform in Fig. 4.9b. Compared with driving the RRM with a single harmonic driving signal, the DE algorithm's combination with the driving signal's shaping offers additional four lines within a 3 dB flatness. For  $N = 1$ , the best compromise flatness/ $L$  is achieved for  $L = 3$  with 0.7 dB flatness when driving the RRM with the solution [ $c_0 = 7$  V,  $V_1 = -7$  V,  $f_0 = 1$  GHz,  $\Delta\lambda = -26$  pm]. The optimized RRM EOFC for  $L = 9$  and  $N = 3$  shows a flatness of 6.8 dB as depicted in Fig. 4.9b.

For a higher number of lines, in the case of  $L = 9$ , the RRM EOFC performs better in flatness than the comb produced by the single harmonic signal, which has a flatness of 10.8 dB for  $L = 7$ . This emphasizes the improvement of using DE optimization to tailor the RRM driving signal. The driving signal features for the optimized 9-line EOFC are presented in Table 4.8 and depicted in Fig. 4.9b.

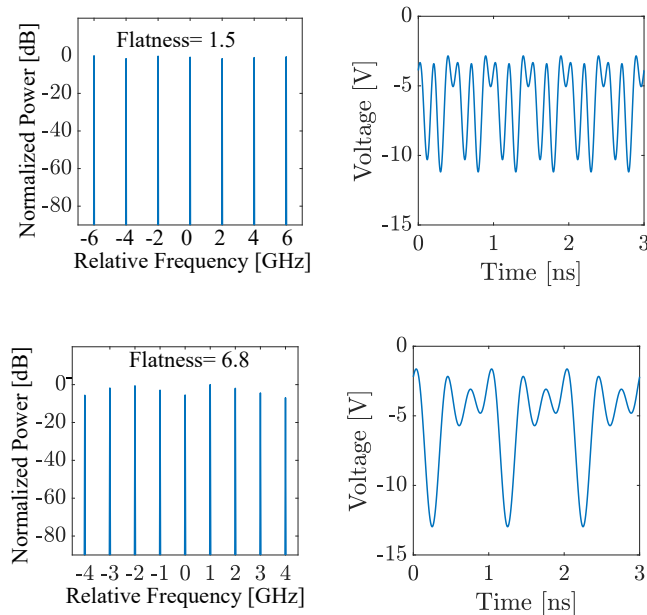


**Figure 4.9.** (a) Numerical optimized 7 lines RRM EOFC using DE algorithm. (b) Optimized driving signal for the 7 lines RRM EOFC. (c) Optimized 9 lines RRM EOFC using DE algorithm. (b) Optimized driving signal for the 9 lines RRM EOFC.

### 4.5.2 Experimental Evaluation RRM EOFC DE Flatness Optimization

The experimental evaluation of the RRM EOFC flatness DE optimization uses the setup in Fig. 4.8. The electrical driving signals found during the numerical analysis are generated using an AWG with a 10-bit resolution and a sampling frequency of 24 GS/s. The AWG maximum generated waveforms have a 1 V peak-to-peak amplitude, and an amplifier is used to provide the levels specified in Table 4.8. Due to limitations over the maximum output power provided by the amplifiers, the numerical amplitude values had to be lowered and manually fine-tuned. Moreover,  $\lambda$  was optimized manually while the driving signal was maintained constant. The fundamental frequency was kept at a lower value of  $f_g = 500$  MHz due to the actual electrical response of the fabricated RRM, which was ignored during the numerical analysis. The discrepancy with the numerical results is due to the simplified model is not tailored to predict the behavior of the fabricated device. For instance, the model considers a phase-shifter based on an ideal abrupt PN junction distributed over the ring's circumference. The experimental optimization values used the optimized numerical solutions as a starting point for manual fine-tuning, which are also described in Table 4.8.

The experimental fine-tuned optimized EOFCS are shown in Fig. 4.10a, and a 7-line comb with 2.9 dB flatness is achieved based on the input waveform of Fig. 4.10b. Additionally, for a 9-line EOFC, a flatness of 5.4 dB is obtained. These results constitute flatness gains and many lines for RRM EOFC reported in the literature [106]. Compared to the DE optimized RRM EOFC driven by a single harmonic driving signal presented in Fig. 4.11, the combination of driving signal shaping and the DE optimization leads to additional four lines within a 3 dB flatness. The DE optimization combined with the tailoring of the RRM can effectively improve the flatness features of RRM EOFCS. Regarding the fundamental frequency, the experimental

**Table 4.8.** Optimized solutions  $\mathbf{x}$  found using the DE algorithm for RRM-based EOFC flatness optimization. DE algorithms coupled with the RRM model ("Num.") and after manual fine-tune optimization considering the DE numerical solutions ("Exp.") for EOFCS containing 7 and 9 lines.

Parameter	Num. ( $L = 7$ )	Num. ( $L = 9$ )	Exp. ( $L = 7$ )	Exp. ( $L = 9$ )
$V_{dc}$ [Volts]	-6.2	-5.3	-7.0	-7.0
$V_1$ [Volts]	1.8	2.6	1.4	1.5
$V_2$ [Volts]	2	2.7	1.5	1.5
$V_3$ [Volts]	2.6	2.4	2.0	1.4
$\phi_1$ [rad]	2.0	3.0	2.0	3.0
$\phi_2$ [rad]	2.8	1.6	2.8	1.6
$f_g$ [GHz]	2.0	1.0	0.5	0.5
$\Delta\lambda$ [pm]	-5	-28	+22	+30
$\delta$ [dB]	1.5	6.8	2.9	5.4

results are suitable for spectroscopy applications. However, DE optimization can benefit other applications, such as optical communication, since frequency is one of the elements within the solutions.

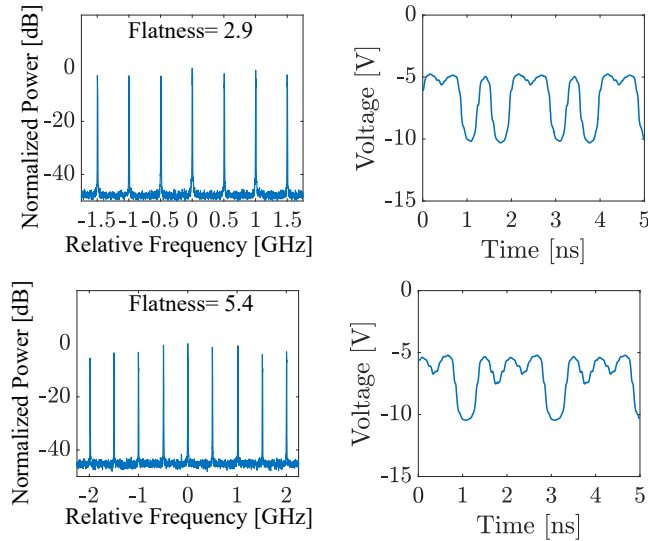


**Figure 4.10.** Measured output spectrums after a manual fine-tune flatness optimization considering the numerical DE solutions as a start point and their corresponding driving voltage signals for the RRM-based EOFCs containing 7 and 9 lines. (a) and (b) represent the output spectrum and the applied voltage as a function of time for the 7-lines EOFC, respectively. (c) and (d) represent the output spectrum and the applied voltage as a function of time for the 9-lines EOFC, respectively.

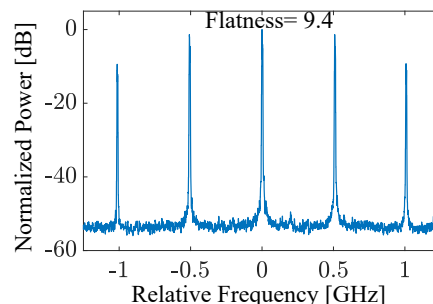


**Figure 4.11.** RRM-based EOFC output spectrum after manual optimization considering a sinusoidal modulation of 500 MHz with an amplitude of  $6.4 \text{ V}_{\text{pp}}$ .

## Summary of the Chapter

This Chapter details the use of DE and PSO gradient-free optimizers for numerical and experimental flatness optimization of EOFCs based on GS-lasers, MZMs, and RRM<sub>s</sub>. Gradient-free optimizers are highly accurate optimization methods that support online optimization directly at the setup. They can overcome limitations such as amplitude noise and restrict the limits of the solution to power-efficient cases. The use of harmonic composition and the algorithms provided flatness gains compared to setups where the devices driving signals are composed of a single harmonic. The results presented in this Chapter can be found in more detail in [20], and we will be expanded in an article on the processing of submission [S1].

# CHAPTER 5

# Reinforcement Learning for EOFC flatness Optimization

---

Reinforcement learning (RL) is a machine learning optimization tool based on the interaction between an agent and an environment and generally guided by improvement of features of a system [107]. In recent years, RL algorithms have gained large applications in optical communications [108, 109], including in the optimization of MMLs operation points [110], ultrafast fiber lasers [111] and self-tuning dissipative solutions [112], but so far RL has not been reported for flatness optimization of EOFCs. There are many RL techniques and algorithms and the choice depends on the problem since they differ in terms of convergence, learning process, compatibility with discreet or continuous action spaces or exploration rate [113].

In this chapter, some results regarding the EOFC flatness optimization using RL algorithms are described, combined with a comparison with the DE gradient-free optimizers described in Chapter 4. The RL algorithms explored are deep deterministic policy gradient, twin delayed DDPG and proximal policy optimization. The RL algorithms explores leads to similar accuracy in terms of flatness performance than the DE while requiring a smaller average demanded time per optimization. On the other hand, DE algorithms possess a higher convergence rate than the RL algorithms explored.

## 5.1 Reinforcement Learning EOFC Optimization Framework

The RL EOFC flatness optimization framework is shown in Fig. 5.1, and it is composed of two parts: the agent and the environment. The environment constitutes the EOFC comb setup based on the GS-laser model of Section 2.2. The DFB laser with the characteristics of Table 2.1 is driven by a signal with waveform generated

by a solution  $\mathbf{x}$  provided by the RL agent. The electrical field generated by the laser passes through a FFT, logarithmic, normalization, and find peaks functions, which determines the peak powers in a fixed frequency window around the EOFC maximum value. The vector  $\mathbf{P}$  with  $L$  peak power values extracted by the finding peaks function also corresponds to the states generated by the solution  $\mathbf{x}$ . The state  $\mathbf{S}$  is given as information to the RL agent together with a reward  $r(\mathbf{x}, \mathbf{S})$ . A state with a flatness profile within a defined target receives the maximum reward, while other profiles are assigned a low reward. The reward is maximum  $r=10$  for  $L=8$  or  $L=9$  lines generated by the GS-laser-based EOFC and  $r=0$  for  $L < 8$ . This methodology incentivizes the RL agent to find solutions that will lead to the maximum reward. In this work, the reward system is based on the number of lines encompassing a 3 dB or 4 dB target flatness.

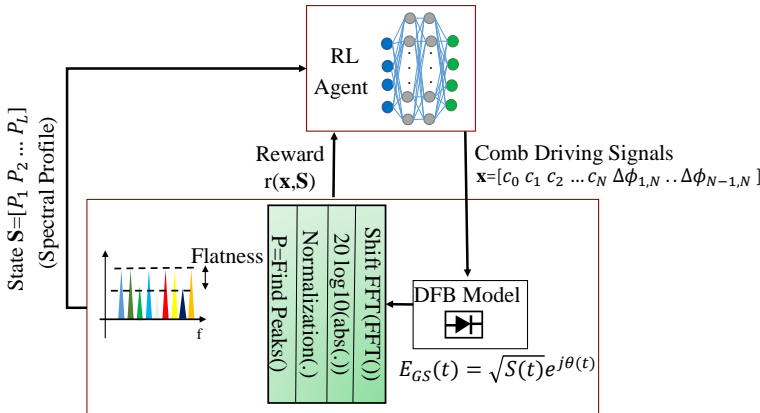


**Figure 5.1.** RL EOFC flatness optimization framework.

The RL agent is represented by an actor and a critic, which are NNs with 2 layers of 800 nodes each. The actor generally predicts the action or solutions  $\mathbf{x}$  to be applied to the DFB laser given an state and a reward from the previous iteration. The critic predicts the discounted long-term reward based on the actions taken. In this work, the RL algorithms applied to the EOFC flatness optimization are: deep deterministic policy gradient (DDPG) [114], twin-delayed deep deterministic policy gradient (TD3) [115] and proximal policy optimization (PPO) [116]. The RL algorithms are implemented using the RL Matlab toolbox and are described in detail in the following sections.

The GS-laser driving signal is composed by three harmonics and relative phases as in Eq. 2.5 with reference in the third harmonic. The RL agent solutions are defined as  $\mathbf{x} = [c_0 \ c_1 \ c_2 \ c_3 \ \Delta\phi_{1,3} \ \Delta\phi_{2,3}]$ . The RF fundamental frequency is  $f_0 = 5$  GHz, and the solutions searching space is limited between 20 to 50 mA for the bias current and the harmonics amplitudes while the relative phases vary from 0 to  $2\pi$ .

### 5.1.1 Deep Deterministic Policy Gradient Algorithm for EOFC flatness optimization

The DDPG is a model-free and online RL algorithm [117]. It suits scenarios where the observation (states) and action space are continuous as it happens for the EOFC flatness optimization. The basic elements of the DDPG algorithm are the actor and critic NNs and a replay buffer [114]. The actor  $NN_{actor}$  is responsible to predict the actions or the EOFC driving signals  $\mathbf{x}$  given an observed state  $\mathbf{S}$  or spectral profile  $\mathbf{P}$ . The critic  $NN_{critic}$  predicts the long-term reward of driving the EOFC with signals  $\mathbf{x}$ . The critic long term reward can be calculated in terms of the Q-value as in

$$Q(\mathbf{x}, \mathbf{S}) = r(\mathbf{x}, \mathbf{S}) + \gamma \max_{\mathbf{x}'} Q(\mathbf{x}', \mathbf{S}'), \quad (5.1)$$

where  $\gamma$  is the discount factor,  $r(\mathbf{x}, \mathbf{S})$  is the reward achieved by the agent in executing action  $\mathbf{x}$  which leads to state  $\mathbf{S}'$  and  $\max_{\mathbf{x}'} Q(\mathbf{x}', \mathbf{S}')$  is the maximum Q-value forecast by the decision made. The replay buffer is used during the calculation and generally stores the data accumulated during these transitions  $(\mathbf{S}, \mathbf{x}, r, \mathbf{S}')$ .

The  $NN_{actor}$  and  $NN_{critic}$  are initialized with random weights, and they are updated for every time step. The actor is trained by maximizing the  $Q(\mathbf{x}, \mathbf{S})$  value of Eq. 5.1. For this, the state is used as input to the actor, while the predicted action and observation is an input for the critic. The training of the critic NN follows the loss function

$$L = (r(\mathbf{x}, \mathbf{S}) + \gamma \max_{\mathbf{x}'} (Q(\mathbf{x}', \mathbf{S}') - Q(\mathbf{x}, \mathbf{S}))^2). \quad (5.2)$$

The calculation of  $\max_{\mathbf{x}'} Q(\mathbf{x}', \mathbf{S}')$  requires an actor to predict the next action  $\mathbf{x}'$  given state  $\mathbf{S}'$  and a critic to predicted the long term reward from these points. If the same critic NN is used to predict both  $Q(\mathbf{x}', \mathbf{S}')$  and  $Q(\mathbf{x}, \mathbf{S})$ , the process is more likely to not converge. Usually, different NN are used and those are called target actor  $NN_{target}^{actor}$  and target critic  $NN_{target}^{critic}$ . The target NNs are used to help the training process.

The  $NN_{actor}^{target}$  and  $NN_{critic}^{target}$  have the same structure and are initialized with the same weights as  $NN_{actor}$  and  $NN_{critic}$ , respectively. The  $NN_{actor}^{target}$  and  $NN_{critic}^{target}$  are frozen during  $NN_{actor}$  and  $NN_{critic}$  training and updated using the values of these networks based on a smoothing factor  $\tau$  varying from 0 to 1. The  $NN_{critic}^{target}$  parameters are updated as [114, 118]

$$NN_{critic}^{target} = \tau NN_{critic} + (1 - \tau) NN_{critic}^{target}, \quad (5.3)$$

while the actor parameters are updated as in [114, 118]

$$NN_{actor}^{target} = \tau NN_{actor} + (1 - \tau) NN_{actor}^{target}. \quad (5.4)$$

At the start of the training, the actor possesses a degree of randomness while taking decisions. The random action allow and the RL agent not to get stuck in the

same pattern and explore the searching space. A stochastic noise is added to the actions taken. As the training progresses, the exploration probability decreases, and the actions tend to be based on the actor predictions.

In the optimization of GS-laser EOFC flatness, per training step, the DDPG agent calculates the comb driving signal features  $\mathbf{x}$  based on the state  $\mathbf{S}$  which contains the vector of peak powers  $\mathbf{P}$ . The laser is driven by the signal  $\mathbf{x}$  and the reward  $r(\mathbf{x}, \mathbf{S})$  and the new state  $\mathbf{S}'$  are extracted. The experience is stored in the relay buffer, which is used by  $\text{NN}_{\text{actor}}^{\text{target}}$  and  $\text{NN}_{\text{critic}}^{\text{target}}$  to calculate the long-term reward. The critic is updated by minimizing the loss in Eq. 5.2. The actor is updated based on a policy gradient method, and the target networks are updated in sequence. The optimization follows in  $N_{\text{epi}}$  episodes and every episode has  $N_{\text{steps}}$  steps. Once the number of steps is reached, a new episode starts. For every episode a random starting point is defined and the experience from previous steps and episodes is stored. The optimization routine is finished once the target flatness is observed in the state. The EOFC flatness optimization DDPG-pseudo algorithm is presented in Algorithm 5 [117].

---

**Algorithm 5:** DDPG RL Algorithm for EOFC flatness optimization

---

```

Initialize  $\text{NN}_{\text{actor}}$  and  $\text{NN}_{\text{critic}}$  with random weights;
Initialize  $\text{NN}_{\text{actor}}^{\text{target}}$  with the same weights as  $\text{NN}_{\text{actor}}$ ;
Initialize  $\text{NN}_{\text{critic}}^{\text{target}}$  with the same weights as  $\text{NN}_{\text{critic}}$ ;
Initialize the replay buffer;
for  $\text{Episode}=1$  until  $N_{\text{epi}}$  do
    Generate a random driving signal and drive the GS-laser;
    Define initial state  $\mathbf{S}$  ;
    for  $\text{Step}=1$  until  $N_{\text{step}}$  do
        Select action  $\mathbf{x}$  using  $\text{NN}_{\text{actor}}$ ;
        Drive the GS-laser with signal  $\mathbf{x}$  and observe reward  $r(\mathbf{x}, \mathbf{S})$  and new
        state  $\mathbf{S}'$ ;
        Store transition  $(\mathbf{S}, \mathbf{x}, r, \mathbf{S}')$  in the buffer;
        Sample random minibatch of  $N_B$  transitions ;
        Calculate the Q-value as in Eq. 5.1;
        Update the  $\text{NN}_{\text{critic}}$  by minimizing the loss in Eq. 5.2;
        Update the  $\text{NN}_{\text{actor}}$  using the sampled policy gradient;
        Update  $\text{NN}_{\text{critic}}^{\text{target}}$  with the weights from  $\text{NN}_{\text{critic}}$  based on Eq. 5.3;
        Update  $\text{NN}_{\text{actor}}^{\text{target}}$  with the weights from  $\text{NN}_{\text{actor}}$  based on Eq. 5.4;
    end
end

```

---

### 5.1.2 Twin-Delayed Deep Deterministic Policy Gradient Algorithm for EOFC flatness optimization

The twin-delayed deep deterministic policy (TD3) is an extension of the DDPG algorithm from Section 5.1.1 [115]. In general, the TD3 has a structure similar to the DDPG algorithm, and is composed of an actor, a critic, and target function approximators. They have the same functions described for the DDPG algorithm and are usually represented by NNs. The TD3 updates  $\text{NN}_{\text{actor}}$  and  $\text{NN}_{\text{critic}}$  at the end of every optimization step. The TD3 algorithm buffer  $B$  stores past experiences learned from the EOFC environment and also adds a stochastic noise to the predicted actions  $\mathbf{x}$  in the initial episodes.

The main difference from the DDPG algorithm is the fact the TD3 algorithm possess two critics  $\text{NN}_{\text{critic},1}$  and  $\text{NN}_{\text{critic},2}$  as well two target critics  $\text{NN}_{\text{critic},1}^{\text{target}}$  and  $\text{NN}_{\text{critic},2}^{\text{target}}$  function approximators. When calculating the Q-value of Eq. 5.1, the chosen value is the minimum between the calculated from the distinct critics [119]. The TD3 agent also updates the RL policy and targets at a lower frequency than the Q-value is updated [120]. Additionally, the TD3 agent adds noise to the target actions  $\mathbf{x}$  to avoid the policy exploring high-value Q-estimates [121].

In the EOFC flatness optimization, the TD3 starts with a random driving signal  $\mathbf{x}$  generating an initial state  $\mathbf{S}$ . The  $\text{NN}_{\text{actor}}$  and  $\text{NN}_{\text{critic},ii}$  are initialized with random values with  $ii = 1, 2$ . The  $\text{NN}_{\text{actor}}^{\text{target}}$  is initialized with the same weights as  $\text{NN}_{\text{actor}}$  while  $\text{NN}_{\text{critic},ii}^{\text{target}}$  received the weights from  $\text{NN}_{\text{critic},ii}$  for  $ii = [1 : 2]$ . For every step, an action  $\mathbf{x}$  is generated based on  $\mathbf{S}$ , a reward  $r$  and the next stage  $\mathbf{S}'$  are observed. The experience is stored in the replay buffer  $B$ . The main difference appears in the calculation of the Q-value where instead of Eq. 5.1, the TD3 algorithm uses [115]

$$Q(\mathbf{x}, \mathbf{S}) = r(\mathbf{x}, \mathbf{S}) + \gamma \min(\text{NN}_{\text{critic},1}, \text{NN}_{\text{critic},2}), \quad (5.5)$$

In Eq. 5.5, the two networks calculate the long-term reward, and the minimum is selected. Consequently, the update of the critic functions depends of their corresponding target approximators, and the loss function becomes

$$L_{ii} = (r(\mathbf{x}, \mathbf{S}) + \gamma \text{NN}_{\text{critic},ii}) - Q_{ii}(\mathbf{x}, \mathbf{S}))^2, \quad (5.6)$$

where  $Q_{ii}(\mathbf{x}, \mathbf{S})$  is the q-value calculated considering the target critic and critic  $ii$ . The TD3 algorithm is presented in Algorithm 6 [115].

---

**Algorithm 6:** TD3 RL algorithm for EOFC flatness optimization

---

```

Initialize  $\text{NN}_{\text{actor}}$ ,  $\text{NN}_{\text{critic},ii}$  with random weights ( $ii = 1 \text{ or } 2$ );
Initialize  $\text{NN}_{\text{actor}}^{\text{target}}$  with the same weights as  $\text{NN}_{\text{actor}}$ ;
Initialize  $\text{NN}_{\text{critic},ii}^{\text{target}}$  with the same weights as  $\text{NN}_{\text{critic},ii}$  ( $ii = 1 \text{ or } 2$ );
Initialize the replay buffer  $B$ ;
for  $\text{Episode}=1$  until  $N_{\text{epi}}$  do
    Generate a random driving signal and drive the GS-laser;
    Define initial state  $\mathbf{S}$  ;
    for  $\text{Step}=1$  until  $N_{\text{step}}$  do
        Select action  $\mathbf{x}$  using  $\text{NN}_{\text{actor}}$ ;
        Drive the GS-laser with signal  $\mathbf{x}$  and observe reward  $r(\mathbf{x}, \mathbf{S})$  and new
        state  $\mathbf{S}'$ ;
        Store transition  $(\mathbf{S}, \mathbf{x}, r, \mathbf{S}')$  in  $B$  ;
        Sample random minibatch of  $N_B$  transitions;
        Calculate the Q-value as in Eq. 5.5 ;
        Update the  $\text{NN}_{\text{critic},ii}$  by minimizing the loss in Eq. 5.6 ;
        Update the  $\text{NN}_{\text{actor}}$  using the sampled policy gradient;
        Update  $\text{NN}_{\text{actor}}^{\text{target}}$  with the weights from  $\text{NN}_{\text{actor}}$ ;
        Update  $\text{NN}_{\text{critic},ii}^{\text{target}}$  with the weights from  $\text{NN}_{\text{critic},ii}$ ;
    end
end

```

---

### 5.1.3 Proximal Policy Optimization Algorithm for EOFC flatness optimization

The PPO is a model-free policy gradient RL algorithm also adequate for continuous action spaces [122]. In the PPO algorithm, the actions taken by the PPO algorithm are selected based on a probability distribution of the state-action long-term reward [123]. The PPO algorithm is suitable for problems with discrete and continuous observation and action spaces and therefore fits the problem of EOFC flatness optimization. The PPO is composed of an actor  $\text{NN}_{\text{actor}}$  and a critic  $\text{NN}_{\text{critic}}$  function approximators. The  $\text{NN}_{\text{actor}}$  calculates the probability of taking an action  $\mathbf{x}$  given the state  $\mathbf{S}$  was observed. In the case of continuous action space as the EOFC driving signals, the decision is based on the mean and standard deviation of the Gaussian probability distribution for the actions. Meanwhile,  $\text{NN}_{\text{critic}}$  returns the long-term reward of the action  $\mathbf{x}$ . The  $\text{NN}_{\text{actor}}$  and  $\text{NN}_{\text{critic}}$  are created with random weights. For every step in the PPO optimization, a sequence of experiences  $(\mathbf{x}, \mathbf{S}, r, \mathbf{S}')$  are created with  $\mathbf{S}'$  being the state observed after action  $\mathbf{x}$  drives the EOFC and  $r$  the associated reward. After observing a state  $\mathbf{S}$ , the agent calculates the probability of actions and selects  $\mathbf{x}$ . The long-term reward can be calculated using a finite horizon [124], or a generalized advantage estimator [123]. The critic is updated using the loss function of Eq. 5.2 and

the actor using the sampled mini-batch data. The PPO simplified pseudo-algorithm for EOFC flatness optimization is shown in Algorithm 7 [123].

---

**Algorithm 7:** PPO RL Algorithm for EOFC flatness optimization

---

```

Initialize NNactor and NNcritic with random weights;
for Episode=1 until Nepi do
    Generate a random driving signal and drive the GS-laser;
    Define initial state  $\mathbf{S}$ ;
    for Step=1 until Nstep do
        Generate a sequence of NPPO experiences following the policy
        NNactor by driving the GS-laser with signal  $\mathbf{x}$  and observing
        the reward r( $\mathbf{x}, \mathbf{S}$ ) and new state  $\mathbf{S}'$ ;
        Calculate the long-term reward using NNcritic;
        Store transitions ( $\mathbf{S}, \mathbf{x}, r, \mathbf{S}'$ ) in the buffer  $B$ ;
    end
    Update the NNcritic by minimizing the loss in Eq. 5.2;
    Update the NNactor using the sampled policy gradient;
end

```

---

#### 5.1.4 Results GS-laser EOFC RL flatness optimization

The GS-laser-based EOFC RL flatness optimization is performed on the setup of Fig. 5.1. The RL agent uses the DDPG, TD3, and PPO algorithms for optimization routines and maximum of 50 cases per algorithm. The maximum number of episodes per optimization case is 10 or 40, i.e., after 10 or 40 episodes the optimization finishes. Each optimization case starts with a new agent without information about the EOFC environment. The episodes have a maximum number of 40 steps. Once the step is finished, the training process is restarted with a new random starting state for the EOFC but with the agent knowledgeable about previously learned points of the routine. The reward system utilizes targets of 3 and 4 dB for the EOFC flatness. For example, EOFC states within a 3 dB flatness receive the maximum reward if the target is a 3 dB flatness.

Considering 50 optimization cases for the DDPG, TD3 and PPO RL algorithms and the DE algorithm of section 4.1.3, a comparison for as EOFC flatness optimization with 4 dB target is shown in Table 5.1. The RL algorithms can find flatness profiles for the defined target but and occasionally fail to find combs with the target flatness profiles during the optimization. The failure in convergence is due to a flawed learning process during the first episodes making the algorithm reinforce a not optimal system of rewards and not finding guesses with better performance. Among the RL algorithms, the DDPG shows to be more suitable for the EOFC optimization with the best convergence rate with 70% convergence in comparison with 54% and 60 % for the TD3 and PPO, respectively. The DDPG agent characteristics are shown in

Table 5.2 while the DE algorithm possesses the hyperparameters  $F = 0.6$ ,  $p_c = 0.8$ ,  $N_c = 40$  and  $N_{ite} = 50$ . In comparison, the DE algorithms are more effective in finding the target solutions and show convergence rate of 100 % for the cases tested. The DE algorithm is not as dependent on the initial starting points since it initializes with solutions uniformly distributed over the searching space. It also keeps a methodology of combining solutions and trial and error along the optimization.

The DE is time demanding and requests longer convergence time when compared with the RL agents, even when considering the optimization of solutions in parallel as explicit in Table 5.1. The parallelization is possible because the analysis considers the EOFC model, but for a sequential process, the time demanded by the DE algorithm is almost 7 times higher. The average number of iterations to convergence is comparatively lower for the RL agents than for the DE algorithm.

**Table 5.1.** RL and DE comparison analysis for the GS-laser EOFC 4 dB Target flatness optimization.

Algorithm	Convergence rate [%]	Average time [min]	Average Iterations
DDPG	70	7.38	2.57
TD3	54	7	2.48
PPO	60	8.83	4
DE (Parallel)	100	29	8.68
DE (Sequential)	100	54	8.68

**Table 5.2.** DDPG Agent properties for the GS-laser based EOFC flatness optimization.

Properties	DDPG Agent
Smooth Factor ( $\tau$ )	$1e - 3$
Mini batch size	64
Discount factor ( $\gamma$ )	0.99
Maximum number of Episodes	10 or 40
Max Steps/Episode	10 or 40
Stop training reward	10

Considering a strict target EOFC flatness of 3 dB, the DDPG RL algorithm can find EOFC with 3 dB flatness target profiles as presented in Table 5.3. The convergence rate decreases compared to the analysis for flatness of 4 dB due to the less availability of solutions with narrower flatness. The 3 dB EOFC profiles are included over the 4 dB optimization. The convergence rate can increase by setting a higher maximum number of episodes per case, as shown in Table 5.3. If the maximum number of episodes per case is increased 4 times, the convergence rate increases 16 %. In this new scenario, the average time demanded for convergence also gets 4 times higher.

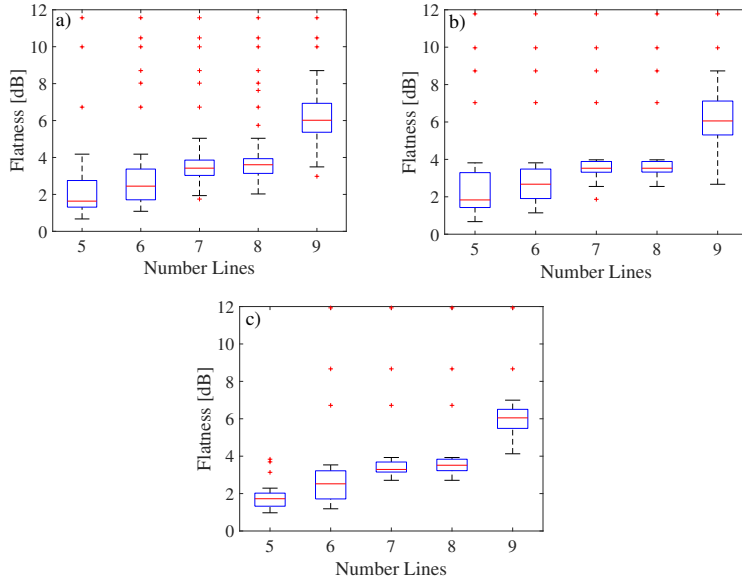


**Figure 5.2.** RL EOFC 4 dB-target flatness optimized distribution (a) DDPG, (b) TD3, (c) PPO.

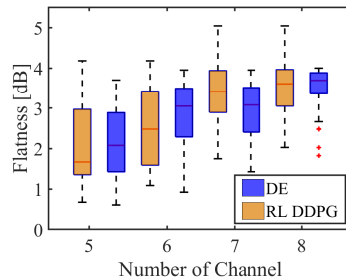


**Figure 5.3.** DE and DDPG comparison EOFC flatness optimization for a 4 dB target.

**Table 5.3.** DDPG analysis for the GS-laser EOFC 3 dB Target flatness optimization.

RL Algorithm	Maximum Episodes/case	Convergence rate [%]	Average time [min]	Average Iterations
DDPG	10	44	12.17	3.77
DDPG	40	60	49	10

The DDPG, TD3 and PPO and DE methodologies lead to a similar performance in terms of flatness optimization of the EOFC as observable in Figs 5.2. The RL approaches lead to comparable flatness distribution while considering the same target

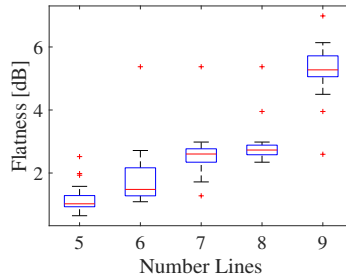


**Figure 5.4.** RL DDPG EOFC 3 dB-target flatness optimized distribution maximum of 10 episodes/optimization case.

EOFC flatness. Differently than the DE optimizer, the RL approach offers an EOFC model with the trained data, and the agent can be re-used for future optimizations with the same target profile. A model is created with stored information about the training process similarly as the inverse system design of Chapter 3 but with online and targeted optimization as the gradient free optimizes. Moreover, the RL approach leads to a shorter optimization time while the gradient-free optimizers have a higher convergence rate. Both methodologies are performed directly on the EOFC setup, which avoids mismatches between numerical models and the available devices. When considering a more restrictive target flatness of 3 dB, the RL approach proves to be accurate as depicted in Fig. 5.4 by using the DDPG algorithm for the optimization.

### 5.1.5 Experimental results DML EOFC DDPG flatness optimization

The experimental validation of the DDPG RL algorithm for EOFC flatness optimization was made considering a NN forward model of the DML(NLK1551SSC) when driven by a multi-harmonic driving signal ( $N = 3$ ). The training data uses as input the vector  $\mathbf{x} = [c_0 \ c_1 \ c_2 \ c_3]$  with  $c_h$  defined as in Eq. 2.5. Meanwhile, the output is the vector containing  $L$  peak power lines from the generated EOFC. The data extraction uses the setup of Fig. 3.6, the searching space for  $N = 3$  of Table 3.4 and follows Algorithm 1. The DML forward model  $NN_{fw}$  is validated similarly as described in Algorithm 2 with the difference that the mapping represents the relationship input/output of the laser. The DDPG RL flatness optimization setup considering  $NN_{fw}$  is depicted in Fig. 5.5.

The average reward for training the EOFC flatness optimization using  $NN_{fw}$  is shown in Fig. 5.6. The RL agent can learn the behavior of the DML laser for targets of 7 and 8 dB over 8 comb lines. The RL optimization follows for 50 iterations, and it can be seen the agent manages to achieve the defined target with less than 10 iterations. Over time, even when the agent leads to non-optimal predictions, it can still recover based on previous experiences.

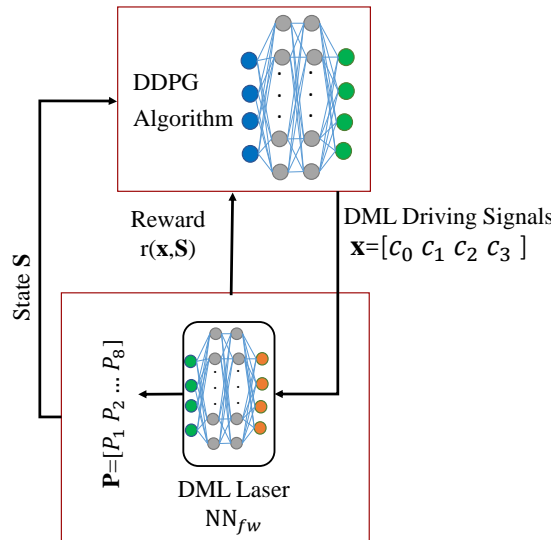


**Figure 5.5.** DDPG RL EOFC flatness optimization using the DML forward model  $NN_{fw}$ .

**Table 5.4.** Optimized hyperparameters for the DML forward model based  $NN_{fw}$  on experimental data.

Models	Output signal	$f_{act}$	$N_{HL}$	$N_{HN}$	$N_{NN}$	$\sigma_{NN}$	$\lambda$
$NN_{fw}$	$\mathbf{P}$	tanh	2	800	100	$8.5 \times 10^{-2}$	$10^8$

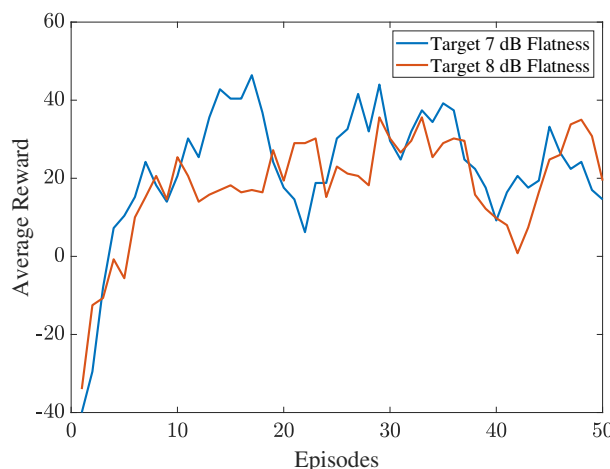


**Figure 5.6.** DDPG RL EOFC flatness optimization using the DML forward model  $NN_{fw}$ .

## Summary of the Chapter

This chapter demonstrates the RL optimization for targeting flatness profiles in EOFCs based on GS-lasers. The DDPG, TD3, and PPO algorithms are validated and present comparable performance in terms of flatness. The RL algorithms led to faster optimization routines than the DE gradient-free optimizer, while the DE shows a higher convergence rate. Both alternatives can be used for online optimization, but the RL agent provides a learning module that can be reused for future optimization over the same EOFC setup.

# CHAPTER 6

# Conclusion

---

The requirements for high-quality EOFCs in applications from metrology to optical communications have motivated the development of this work. EOFCs are highly flexible and efficient for comb generation, and the current limitations in spectral broadening, bandwidth, and elevated driving signals can be compensated by applied ML optimization techniques. Moreover, to be aligned with future autonomous system applications, accurate optimization techniques can save time and avoid sub-optimal fine-tuning of the EOFC operation. ML algorithms have the potential to increase the performance of the combs. The ML methods provide an alternative for autonomous EOFC optimization that can support flexible and optimal applications of EOFCs while expanding their capabilities. The algorithms presented in this work include an inverse system mapping for accurate comb representation, online optimization algorithms, and a reinforcement learning module that actively interacts with the EOFC environment and, while leading to the achievement of target spectral profiles, also learning the system behavior. In this Chapter, a summary of the results and contributions presented in this work are described, and future research perspectives are pointed out.

## 6.1 Summary

The optimization machine techniques for EOFCs led to the following results:

- **Benchmark for automated EOFC optimization:** Online and offline optimization frameworks for EOFC are proposed and numerically and experimentally studied. The ML techniques explored manage to cope with EOFC limitations such as amplitude noise, devices bandwidth, and low CNR. Two gradient-free algorithms are evaluated. Real-time optimization tools support autonomous systems, save time demanded to fine-tune EOFC with many degrees of freedom, and, combined with theoretical approaches, can push the limit for EOFC performance. ML reduces processing time for real-time automatizing.
- **Approximated accurate models and prediction for EOFC flatness optimization:** An inverse system model and RL agent model for EOFCs were validated and supported a characterization of an EOFC produced by a GS-laser. The model accurately predicts the driving signals for arbitrary spectral profiles

and can be used as a simulation tool fitted to a device behavior or to assess an EOFC performance. Additionally, the model can be used to target determined EOFC spectral shaping.

- **Driving signal shaping to improve the flatness of EOFC based on GS-lasers:** The use of signal composition is shown numerically and experimentally to improve the flatness performance of EOFCs based only on a GS-laser. Shaping the laser and modulator driving signals are a powerful asset for performance improvement, especially when optimized using ML techniques.
- **Enable power and cost-efficient EOFC generation:** ML algorithms can potentially serve as a methodology for power-efficient EOFC generation. The techniques presented allow restrictions over prohibitive energy-expensive signal amplitudes, as can be found in the literature for EOFC modulators.

## 6.2 Outlook

Perspectives for future research on the topic are:

The inverse system model of Chapter 3 faces limitations in training and validation when the laser driving signals are composed of multiple harmonics and phases combined. The multiple-to-one map is the biggest challenge for training the model. The technique can be extended to compensate for the impairment or learn accurately while including the phases. As presented in Chapter 4, adding the phases to the laser driving signal brings a significant gain over the resulting EOFC flatness.

In the use of gradient-free optimizers of Chapter 4, the main challenge is to cope with the amplitude noise in the comb peak powers. Since the optimization fitness function relies on the vector of comb peak powers, a stable and low amplitude variation is crucial for achieving the target spectrum. A scheme with amplitude noise pre-compensation can potentially improve the algorithm's performance. Besides, evaluating the impact of phase noise in the EOFC-generated comb is also crucial for comb applications. Some attempts were made to optimize semiconductor optical amplifiers based on combs. Still, limitations in the time demanded the numerical optimization prevented a deeper analysis, and further investigation is relevant [125].

The RL framework of Chapter 5 requires experimental validation in a setup, especially for analysis of the technique when dealing with amplitude noise and setup instabilities.

Overall, the reported results demonstrate how ML techniques improve the performance of EOFC with defined target features. The algorithms are useful for complex systems employing EOFCs, and integration of the EOFC optimization tools is an advantage for these systems.

# Bibliography

---

- [1] J. Schröder, A. Fülöp, M. Mazur, L. Lundberg, Ó. B. Helgason, M. Karlsson, P. A. Andrekson, *et al.*, “Laser frequency combs for coherent optical communications,” *Journal of Lightwave Technology*, vol. 37, no. 7, pp. 1663–1670, 2019.
- [2] P. Marin-Palomo, J. N. Kemal, T. J. Kippenberg, W. Freude, S. Randel, and C. Koos, “Performance of chip-scale optical frequency comb generators in coherent wdm communications,” *Optics express*, vol. 28, no. 9, pp. 12897–12910, 2020.
- [3] T. Udem, R. Holzwarth, and T. W. Hänsch, “Optical frequency metrology,” *Nature*, vol. 416, no. 6877, pp. 233–237, 2002.
- [4] I. Coddington, N. Newbury, and W. Swann, “Dual-comb spectroscopy,” *Optica*, vol. 3, no. 4, pp. 414–426, 2016.
- [5] N. Kuse and M. E. Fermann, “Frequency-modulated comb lidar,” *Apl Photonics*, vol. 4, no. 10, p. 106105, 2019.
- [6] M.-G. Suh, X. Yi, Y.-H. Lai, S. Leifer, I. S. Grudinin, G. Vasisht, E. C. Martin, M. P. Fitzgerald, G. Doppmann, J. Wang, *et al.*, “Searching for exoplanets using a microresonator astrocomb,” *Nature photonics*, vol. 13, no. 1, pp. 25–30, 2019.
- [7] J. L. Hall, “Nobel lecture: Defining and measuring optical frequencies,” *Reviews of modern physics*, vol. 78, no. 4, p. 1279, 2006.
- [8] T. W. Hänsch, “Nobel lecture: passion for precision,” *Reviews of Modern Physics*, vol. 78, no. 4, p. 1297, 2006.
- [9] J. Kim and Y. Song, “Ultralow-noise mode-locked fiber lasers and frequency combs: principles, status, and applications,” *Advances in Optics and Photonics*, vol. 8, no. 3, pp. 465–540, 2016.
- [10] T. Yang, J. Dong, S. Liao, D. Huang, and X. Zhang, “Comparison analysis of optical frequency comb generation with nonlinear effects in highly nonlinear fibers,” *Optics express*, vol. 21, no. 7, pp. 8508–8520, 2013.

- [11] A. Parriaux, K. Hammani, and G. Millot, “Electro-optic frequency combs,” *Advances in Optics and Photonics*, vol. 12, no. 1, pp. 223–287, 2020.
- [12] T. Fortier and E. Baumann, “20 years of developments in optical frequency comb technology and applications,” *Communications Physics*, vol. 2, no. 1, pp. 1–16, 2019.
- [13] L. Hargrove, R. L. Fork, and M. Pollack, “Locking of he–ne laser modes induced by synchronous intracavity modulation,” *Applied Physics Letters*, vol. 5, no. 1, pp. 4–5, 1964.
- [14] A. Rosado, A. Perez-Serrano, J. M. G. Tijero, A. Valle, L. Pesquera, and I. Esquivias, “Experimental study of optical frequency comb generation in gain-switched semiconductor lasers,” *Optics & Laser Technology*, vol. 108, pp. 542–550, 2018.
- [15] S. Ozharar, F. Quinlan, I. Ozdur, S. Gee, and P. Delfyett, “Ultraflat optical comb generation by phase-only modulation of continuous-wave light,” *IEEE photonics technology letters*, vol. 20, no. 1, pp. 36–38, 2007.
- [16] Q. Wang, L. Huo, Y. Xing, and B. Zhou, “Ultra-flat optical frequency comb generator using a single-driven dual-parallel mach–zehnder modulator,” *Optics Letters*, vol. 39, no. 10, pp. 3050–3053, 2014.
- [17] Y. Cui, Z. Wang, Y. Xu, Y. Jiang, J. Yu, and Z. Huang, “Generation of flat optical frequency comb using cascaded pms with combined harmonics,” *IEEE Photonics Technology Letters*, 2022.
- [18] A. Delmade, M. Krstić, C. Browning, J. Crnjanski, D. Gvozdić, and L. Barry, “Power efficient optical frequency comb generation using laser gain switching and dual-drive mach-zehnder modulator,” *Optics Express*, vol. 27, no. 17, pp. 24135–24146, 2019.
- [19] N. Yokota, K. Abe, S. Mieda, and H. Yasaka, “Harmonic superposition for tailored optical frequency comb generation by a mach–zehnder modulator,” *Optics letters*, vol. 41, no. 5, pp. 1026–1029, 2016.
- [20] T. Pinto, U. C. De Moura, F. Da Ros, M. Krstić, J. V. Crnjanski, A. Napoli, D. M. Gvozdić, and D. Zibar, “Optimization of frequency combs spectral-flatness using evolutionary algorithm,” *Optics Express*, vol. 29, no. 15, pp. 23447–23460, 2021.
- [21] D. Zibar, A. M. R. Brusin, U. C. de Moura, F. Da Ros, V. Curri, and A. Carena, “Inverse system design using machine learning: the raman amplifier case,” *Journal of Lightwave Technology*, vol. 38, no. 4, pp. 736–753, 2019.

- [22] A. Rosado, A. Pérez-Serrano, J. M. G. Tijero, Á. Valle, L. Pesquera, and I. Esquivias, “Enhanced optical frequency comb generation by pulsed gain-switching of optically injected semiconductor lasers,” *Optics express*, vol. 27, no. 6, pp. 9155–9163, 2019.
- [23] T. Sakamoto, T. Kawanishi, and M. Izutsu, “Widely wavelength-tunable ultra-flat frequency comb generation using conventional dual-drive mach-zehnder modulator,” *Electronics Letters*, vol. 43, no. 19, p. 1, 2007.
- [24] T. Sakamoto, T. Kawanishi, and M. Tsuchiya, “10 ghz, 2.4 ps pulse generation using a single-stage dual-drive mach-zehnder modulator,” *Optics letters*, vol. 33, no. 8, pp. 890–892, 2008.
- [25] K.-P. Ho and J. M. Kahn, “Optical frequency comb generator using phase modulation in amplified circulating loop,” *IEEE photonics technology letters*, vol. 5, no. 6, pp. 721–725, 1993.
- [26] K. Qu, S. Zhao, X. Li, Z. Zhu, D. Liang, and D. Liang, “Ultra-flat and broadband optical frequency comb generator via a single mach–zehnder modulator,” *IEEE Photonics Technology Letters*, vol. 29, no. 2, pp. 255–258, 2016.
- [27] C. He, S. Pan, R. Guo, Y. Zhao, and M. Pan, “Ultraflat optical frequency comb generated based on cascaded polarization modulators,” *Optics letters*, vol. 37, no. 18, pp. 3834–3836, 2012.
- [28] Y. Yang, J. Ma, X. Xin, Q. Zhang, Y. Zhang, X. Yin, R. Zhang, and W. Liu, “Optical frequency comb generation using two cascaded polarization modulators,” *Photonic Network Communications*, vol. 32, no. 1, pp. 126–132, 2016.
- [29] Y. Dou, H. Zhang, and M. Yao, “Generation of flat optical-frequency comb using cascaded intensity and phase modulators,” *IEEE Photonics Technology Letters*, vol. 24, no. 9, pp. 727–729, 2012.
- [30] K. Kashiwagi, T. Kurokawa, Y. Okuyama, T. Mori, Y. Tanaka, Y. Yamamoto, and M. Hirano, “Direct generation of 12.5-ghz-spaced optical frequency comb with ultrabroad coverage in near-infrared region by cascaded fiber configuration,” *Optics Express*, vol. 24, no. 8, pp. 8120–8131, 2016.
- [31] I. L. Gheorma and G. K. Gopalakrishnan, “Flat frequency comb generation with an integrated dual-parallel modulator,” *IEEE Photonics Technology Letters*, vol. 19, no. 13, pp. 1011–1013, 2007.
- [32] J. Li, H. Ma, Z. Li, and X. Zhang, “Optical frequency comb generation based on dual-polarization iq modulator shared by two polarization-orthogonal recirculating frequency shifting loops,” *IEEE Photonics Journal*, vol. 9, no. 5, pp. 1–10, 2017.

- [33] N. B. Hébert, V. Michaud-Belleau, C. Perrella, G.-W. Truong, J. D. Anstie, T. M. Stace, J. Genest, and A. N. Luiten, “Real-time dynamic atomic spectroscopy using electro-optic frequency combs,” *Physical Review Applied*, vol. 6, no. 4, p. 044012, 2016.
- [34] S. Schiller, “Spectrometry with frequency combs,” *Optics letters*, vol. 27, no. 9, pp. 766–768, 2002.
- [35] L. Lundberg, M. Karlsson, A. Lorences-Riesgo, M. Mazur, V. Torres-Company, J. Schröder, and P. A. Andrekson, “Frequency comb-based wdm transmission systems enabling joint signal processing,” *Applied Sciences*, vol. 8, no. 5, p. 718, 2018.
- [36] B. Vikram, R. Prakash, K. Nagarjun, A. Singh, S. K. Selvaraja, and V. Supradeepa, “Generation of a multi-wavelength source spanning the entire c-band by nonlinear spectral broadening of dual-carrier electro-optic frequency combs,” *OSA Continuum*, vol. 3, no. 8, pp. 2185–2194, 2020.
- [37] J. Li, J. Lin, X. Zhang, L. Xi, X. Tang, and Y. Qiao, “Scheme for generation of flat top and high signal-to-noise ratio optical frequency comb,” *Chinese Optics Letters*, vol. 13, no. 1, pp. 010605–010605, 2015.
- [38] T. Keating, X. Jin, S. L. Chuang, and K. Hess, “Temperature dependence of electrical and optical modulation responses of quantum-well lasers,” *IEEE journal of quantum electronics*, vol. 35, no. 10, pp. 1526–1534, 1999.
- [39] L. A. Coldren, S. W. Corzine, and M. L. Mashanovitch, *Diode lasers and photonic integrated circuits*, vol. 218. John Wiley & Sons, 2012.
- [40] R. Nagarajan, M. Ishikawa, T. Fukushima, R. S. Geels, and J. E. Bowers, “High speed quantum-well lasers and carrier transport effects,” *IEEE Journal of Quantum Electronics*, vol. 28, no. 10, pp. 1990–2008, 1992.
- [41] R.-K. Shiu, Y.-W. Chen, P.-C. Peng, J. Chiu, Q. Zhou, T.-L. Chang, S. Shen, J.-W. Li, and G.-K. Chang, “Performance enhancement of optical comb based microwave photonic filter by machine learning technique,” *Journal of Lightwave Technology*, vol. 38, no. 19, pp. 5302–5310, 2020.
- [42] M. Seimetz, *High-order modulation for optical fiber transmission*, vol. 143. Springer, 2009.
- [43] K. P. Nagarjun, V. Jeyaselvan, S. K. Selvaraja, and V. R. Supradeepa, “Generation of tunable, high repetition rate optical frequency combs using on-chip silicon modulators,” *Optics Express*, vol. 26, no. 8, pp. 10744–10753, 2018.
- [44] K. P. Nagarjun, R. Prakash, B. S. Vikram, S. Arora, V. Jeyaselvan, S. K. Selvaraja, and V. R. Supradeepa, “Bandwidth scaling of silicon modulator-based combs using multi-carriers and frequency offset locking,” *OSA Continuum*, vol. 3, no. 4, pp. 921–928, 2020.

- [45] J. Lin, H. Sepehrian, Y. Xu, L. A. Rusch, and W. Shi, "Frequency comb generation using a cmos compatible sip dd-mzm for flexible networks," *IEEE Photonics Technology Letters*, vol. 30, pp. 1495–1498, 2018.
- [46] Z. Wang, M. Ma, H. Sun, M. Khalil, R. Adams, K. Yim, X. Jin, and L. R. Chen, "Optical frequency comb generation using cmos compatible cascaded mach-zehnder modulators," *IEEE Journal of Quantum Electronics*, vol. 55, pp. 1–6, 2019.
- [47] S. Liu, K. Wu, L. Zhou, L. Lu, B. Zhang, G. Zhou, and J. Chen, "Microwave pulse generation with a silicon dual-parallel modulator," *Journal of Lightwave Technology*, vol. 38, pp. 2134–2143, 2020.
- [48] X. Wu and H. K. Tsang, "Flat-top frequency comb generation with silicon microring modulator and filter," in *Conference on Lasers and Electro-Optics*, p. SM4O.6, Optical Society of America, 2017.
- [49] I. Demirtzioglou, C. Lacava, K. R. H. Bottrill, D. J. Thomson, G. T. Reed, D. J. Richardson, and P. Petropoulos, "Frequency comb generation in a silicon ring resonator modulator," *Optics Express*, vol. 26, no. 2, pp. 790–796, 2018.
- [50] N. K. P., P. Raj, V. Jeyaselvan, S. K. Selvaraja, and V. R. Supradeepa, "Observation of novel optical and microwave power dependent effects in silicon micro-ring modulator based frequency comb generators," in *Laser Resonators, Microresonators, and Beam Control XXI* (A. V. Kudryashov, A. H. Paxton, and V. S. Ilchenko, eds.), vol. 10904, pp. 77 – 83, International Society for Optics and Photonics, SPIE, 2019.
- [51] Y. Xu, J. Lin, R. Dubé-Demers, S. LaRochelle, L. Rusch, and W. Shi, "Integrated flexible-grid wdm transmitter using an optical frequency comb in microring modulators," *Optics Letters*, vol. 43, no. 7, pp. 1554–1557, 2018.
- [52] K. P. Nagarjun, P. Raj, V. Jeyaselvan, S. K. Selvaraja, and V. R. Supradeepa, "Microwave power induced resonance shifting of silicon ring modulators for continuously tunable, bandwidth scaled frequency combs," *Optics Express*, vol. 28, no. 9, pp. 13032–13042, 2020.
- [53] W. D. Sacher and J. K. Poon, "Dynamics of microring resonator modulators," *Optics express*, vol. 16, no. 20, pp. 15741–15753, 2008.
- [54] R. Dubé-Demers, J. St-Yves, A. Bois, Q. Zhong, M. Caverley, Y. Wang, L. Chrostowski, S. LaRochelle, D. V. Plant, and W. Shi, "Analytical modeling of silicon microring and microdisk modulators with electrical and optical dynamics," *Journal of Lightwave Technology*, vol. 33, no. 20, pp. 4240–4252, 2015.
- [55] R. Soref and B. Bennett, "Electrooptical effects in silicon," *IEEE journal of quantum electronics*, vol. 23, no. 1, pp. 123–129, 1987.

- [56] D. Marris-Morini, L. Vivien, G. Rasigade, J.-M. Fedeli, E. Cassan, X. Le Roux, P. Crozat, S. Maine, A. Lupu, P. Lyan, *et al.*, “Recent progress in high-speed silicon-based optical modulators,” *Proceedings of the IEEE*, vol. 97, no. 7, pp. 1199–1215, 2009.
- [57] A. B. Fallahkhair, K. S. Li, and T. E. Murphy, “Vector finite difference modesolver for anisotropic dielectric waveguides,” *Journal of lightwave technology*, vol. 26, no. 11, pp. 1423–1431, 2008.
- [58] X. Wang, P. O. Weigel, J. Zhao, M. Ruesing, and S. Mookherjea, “Achieving beyond-100-ghz large-signal modulation bandwidth in hybrid silicon photonics mach zehnder modulators using thin film lithium niobate,” *APL Photonics*, vol. 4, no. 9, p. 096101, 2019.
- [59] W. Heni, C. Haffner, B. Baeuerle, Y. Fedoryshyn, A. Josten, D. Hillerkuss, J. Niegemann, A. Melikyan, M. Kohl, D. Elder, *et al.*, “108 gbit/s plasmonic mach–zehnder modulator with > 70-ghz electrical bandwidth,” *Journal of Lightwave Technology*, vol. 34, no. 2, pp. 393–400, 2016.
- [60] R. Zhou, T. N. Huynh, V. Vujicic, P. M. Anandarajah, and L. P. Barry, “Phase noise analysis of injected gain switched comb source for coherent communications,” *Optics Express*, vol. 22, no. 7, pp. 8120–8125, 2014.
- [61] R. T. Watts, S. G. Murdoch, and L. P. Barry, “Phase noise reduction of an optical frequency comb using a feed-forward heterodyne detection scheme,” *IEEE Photonics Journal*, vol. 8, no. 1, pp. 1–7, 2016.
- [62] M. Endo, T. D. Shoji, and T. R. Schibli, “Ultralow noise optical frequency combs,” *IEEE Journal of Selected Topics in Quantum Electronics*, vol. 24, no. 5, pp. 1–13, 2018.
- [63] K. Saleh and Y. Chembo, “Phase noise performance comparison between microwaves generated with kerr optical frequency combs and optoelectronic oscillators,” *Electronics Letters*, vol. 53, no. 4, pp. 264–266, 2017.
- [64] R. Wu, V. Supradeepa, C. M. Long, D. E. Leaird, and A. M. Weiner, “Generation of very flat optical frequency combs from continuous-wave lasers using cascaded intensity and phase modulators driven by tailored radio frequency waveforms,” *Optics letters*, vol. 35, no. 19, pp. 3234–3236, 2010.
- [65] J. Zhang, J. Yu, N. Chi, Z. Dong, X. Li, Y. Shao, J. Yu, and L. Tao, “Flattened comb generation using only phase modulators driven by fundamental frequency sinusoidal sources with small frequency offset,” *Optics letters*, vol. 38, no. 4, pp. 552–554, 2013.
- [66] L. Chang, S. Liu, and J. E. Bowers, “Integrated optical frequency comb technologies,” *Nature Photonics*, vol. 16, no. 2, pp. 95–108, 2022.

- [67] N. Yokota and H. Yasaka, “Operation strategy of inp mach–zehnder modulators for flat optical frequency comb generation,” *IEEE Journal of Quantum Electronics*, vol. 52, no. 8, pp. 1–7, 2016.
- [68] R. Slavík, S. G. Farwell, M. J. Wale, and D. J. Richardson, “Compact optical comb generator using inp tunable laser and push-pull modulator,” *IEEE Photonics Technology Letters*, vol. 27, no. 2, pp. 217–220, 2014.
- [69] N. Andriolli, T. Cassese, M. Chiesa, C. De Dios, and G. Contestabile, “Photonic integrated fully tunable comb generator cascading optical modulators,” *Journal of Lightwave Technology*, vol. 36, no. 23, pp. 5685–5689, 2018.
- [70] F. Bontempi, N. Andriolli, F. Scotti, M. Chiesa, and G. Contestabile, “Comb line multiplication in an inp integrated photonic circuit based on cascaded modulators,” *IEEE Journal of Selected Topics in Quantum Electronics*, vol. 25, no. 6, pp. 1–7, 2019.
- [71] T. Ren, M. Zhang, C. Wang, L. Shao, C. Reimer, Y. Zhang, O. King, R. Esman, T. Cullen, and M. Lončar, “An integrated low-voltage broadband lithium niobate phase modulator,” *IEEE Photonics Technology Letters*, vol. 31, no. 11, pp. 889–892, 2019.
- [72] S. Liu, K. Wu, L. Zhou, L. Lu, B. Zhang, G. Zhou, and J. Chen, “Optical frequency comb and nyquist pulse generation with integrated silicon modulators,” *IEEE Journal of Selected Topics in Quantum Electronics*, vol. 26, no. 2, pp. 1–8, 2019.
- [73] A. Kokhanovskiy, E. Kuprikov, A. Bednyakova, I. Popkov, S. Smirnov, and S. Turitsyn, “Inverse design of mode-locked fiber laser by particle swarm optimization algorithm,” *Scientific reports*, vol. 11, no. 1, pp. 1–9, 2021.
- [74] E. Lucas, S.-P. Yu, G. H. Ahn, K. Yang, J. Vuckovic, and S. B. Papp, “Inverse spectral design of kerr microcomb pulses,” in *Laser Resonators, Microresonators, and Beam Control XXIII*, vol. 11672, p. 1167205, SPIE, 2021.
- [75] D. Zibar, A. Ferrari, V. Curri, and A. Carena, “Machine learning-based raman amplifier design,” in *Optical Fiber Communication Conference*, pp. M1J–1, Optical Society of America, 2019.
- [76] X. Xu, C. Sun, Y. Li, J. Zhao, J. Han, and W. Huang, “An improved tandem neural network for the inverse design of nanophotonics devices,” *Optics Communications*, vol. 481, p. 126513, 2021.
- [77] P. Li *et al.*, “Inverse design of programmable optical frequency comb using deep learning,” *Journal of Optics*, 2022.

- [78] J. Wen, W. Qin, W. Sun, C. He, K. Xiong, and B. Liang, “Machine learning regression approach to on-chip optical frequency combs analyses,” *Optical Engineering*, vol. 60, no. 12, p. 124101, 2021.
- [79] X. Ma, J. Lin, C. Dai, J. Lv, P. Yao, L. Xu, and C. Gu, “Machine learning method for calculating mode-locking performance of linear cavity fiber lasers,” *Optics & Laser Technology*, vol. 149, p. 107883, 2022.
- [80] A. Kokhanovskiy, A. Bednyakova, E. Kuprikov, A. Ivanenko, M. Dyatlov, D. Lotkov, S. Kobtsev, and S. Turitsyn, “Machine learning-based pulse characterization in figure-eight mode-locked lasers,” *Optics Letters*, vol. 44, no. 13, pp. 3410–3413, 2019.
- [81] U. C. de Moura, F. Da Ros, A. M. R. Brusin, A. Carena, and D. Zibar, “Experimental characterization of raman amplifier optimization through inverse system design,” *Journal of Lightwave Technology*, vol. 39, no. 4, pp. 1162–1170, 2020.
- [82] M. Ionescu, “Machine learning for ultrawide bandwidth amplifier configuration,” in *2019 21st International Conference on Transparent Optical Networks (ICTON)*, pp. 1–4, IEEE, 2019.
- [83] X. Ye, A. Arnould, A. Ghazisaeidi, D. Le Gac, and J. Renaudier, “Experimental prediction and design of ultra-wideband raman amplifiers using neural networks,” in *Optical Fiber Communication Conference*, pp. W1K–3, Optica Publishing Group, 2020.
- [84] U. C. De Moura, M. A. Iqbal, M. Kamalian, L. Krzczanowicz, F. Da Ros, A. M. R. Brusin, A. Carena, W. Forysiak, S. Turitsyn, and D. Zibar, “Multi-band programmable gain raman amplifier,” *Journal of Lightwave Technology*, vol. 39, no. 2, pp. 429–438, 2020.
- [85] Y. Chen, J. Du, Y. Huang, K. Xu, and Z. He, “Intelligent gain flattening in wavelength and space domain for fmf raman amplification by machine learning based inverse design,” *Optics Express*, vol. 28, no. 8, pp. 11911–11920, 2020.
- [86] M. Soltani, F. Da Ros, A. Carena, and D. Zibar, “Inverse design of a raman amplifier in frequency and distance domains using convolutional neural networks,” *Optics letters*, vol. 46, no. 11, pp. 2650–2653, 2021.
- [87] A. Quirce, A. Rosado, J. Díez, A. Valle, A. Pérez-Serrano, J.-M. G. Tijero, L. Pesquera, and I. Esquivias, “Nonlinear dynamics induced by optical injection in optical frequency combs generated by gain-switching of laser diodes,” *IEEE Photonics Journal*, vol. 12, no. 4, pp. 1–14, 2020.
- [88] A. Rosado, A. Pérez-Serrano, J. M. G. Tijero, A. V. Gutierrez, L. Pesquera, and I. Esquivias, “Numerical and experimental analysis of optical frequency comb generation in gain-switched semiconductor lasers,” *IEEE Journal of Quantum Electronics*, vol. 55, no. 6, pp. 1–12, 2019.

- [89] J. N. Kutz and S. L. Brunton, “Machine learning for self-tuning optical systems,” in *Nonlinear Optics*, pp. NTh1A–1, Optical Society of America, 2019.
- [90] U. de Moura, T. Monteiro, A. M. Brusin†, A. Carena, D. Napoli, Antonio Zibar, and F. Da Ros, “Online versus offline optimization methods for raman amplifier optimization,” in *27th OptoElectronics and Communications Conference/International Conference on Photonics in Switching and Computing (OECC/PSC) 2022*.
- [91] B. Fischer, M. Chemnitz, B. Maclellan, P. Roztocki, R. Helsten, B. Wetzel, B. E. Little, S. T. Chu, D. J. Moss, J. Azaña, *et al.*, “Autonomous on-chip interferometry for reconfigurable optical waveform generation,” *Optica*, vol. 8, no. 10, pp. 1268–1276, 2021.
- [92] T. T. Tran, M. Song, M. Song, and D. Seo, “Highly flat optical frequency comb generation based on pulse carving and sinusoidal phase modulation,” *Optical engineering*, vol. 58, no. 7, p. 076103, 2019.
- [93] S. Chen, S. A. Billings, and P. Grant, “Non-linear system identification using neural networks,” *International journal of control*, vol. 51, no. 6, pp. 1191–1214, 1990.
- [94] G.-B. Huang, Q.-Y. Zhu, and C.-K. Siew, “Extreme learning machine: theory and applications,” *Neurocomputing*, vol. 70, no. 1-3, pp. 489–501, 2006.
- [95] C. Jayne, A. Lanitis, and C. Christodoulou, “Neural network methods for one-to-many multi-valued mapping problems,” *Neural Computing and Applications*, vol. 20, no. 6, pp. 775–785, 2011.
- [96] G. F. Pendiuk, P. T. Neves, and A. A. Pohl, “Use of a differential evolution algorithm for determining input driving signals in optical frequency combs,” *OSA Continuum*, vol. 3, no. 8, pp. 2232–2242, 2020.
- [97] R. Poli, J. Kennedy, and T. Blackwell, “Particle swarm optimization,” *Swarm intelligence*, vol. 1, no. 1, pp. 33–57, 2007.
- [98] K. V. Price, “Differential evolution,” in *Handbook of optimization*, pp. 187–214, Springer, 2013.
- [99] Q. Bai, “Analysis of particle swarm optimization algorithm,” *Computer and information science*, vol. 3, no. 1, p. 180, 2010.
- [100] Y. Zhang, S. Wang, and G. Ji, “A comprehensive survey on particle swarm optimization algorithm and its applications,” *Mathematical Problems in Engineering*, vol. 2015, 2015.
- [101] J. Kennedy and R. Eberhart, “Particle swarm optimization,” in *Proceedings of ICNN’95-international conference on neural networks*, vol. 4, pp. 1942–1948, IEEE, 1995.

- [102] S. Koziel and X.-S. Yang, *Computational optimization, methods and algorithms*, vol. 356. Springer, 2011.
- [103] K. Price, R. M. Storn, and J. A. Lampinen, *Differential evolution: a practical approach to global optimization*. Springer Science & Business Media, 2006.
- [104] D. Corne, M. Dorigo, F. Glover, D. Dasgupta, P. Moscato, R. Poli, and K. V. Price, *New ideas in optimization*. McGraw-Hill Ltd., UK, 1999.
- [105] Y. Xu, J. Lin, R. Dubé-Demers, S. LaRochelle, L. Rusch, and W. Shi, “Integrated flexible-grid wdm transmitter using an optical frequency comb in microring modulators,” *Optics letters*, vol. 43, no. 7, pp. 1554–1557, 2018.
- [106] I. Demirtzioglou, C. Lacava, K. R. Bottrill, D. J. Thomson, G. T. Reed, D. J. Richardson, and P. Petropoulos, “Frequency comb generation in a silicon ring resonator modulator,” *Optics express*, vol. 26, no. 2, pp. 790–796, 2018.
- [107] L. P. Kaelbling, M. L. Littman, and A. W. Moore, “Reinforcement learning: A survey,” *Journal of artificial intelligence research*, vol. 4, pp. 237–285, 1996.
- [108] R. Weixer, S. Kühl, R. M. Morais, B. Spinnler, W. Schairer, B. Sommerkorn-Krombholz, and S. Pachnicke, “A reinforcement learning framework for parameter optimization in elastic optical networks,” in *2020 European Conference on Optical Communications (ECOC)*, pp. 1–4, IEEE, 2020.
- [109] Y. Qian, J. Wu, R. Wang, F. Zhu, and W. Zhang, “Survey on reinforcement learning applications in communication networks,” *Journal of Communications and Information Networks*, vol. 4, no. 2, pp. 30–39, 2019.
- [110] C. Sun, E. Kaiser, S. L. Brunton, and J. N. Kutz, “Deep reinforcement learning for optical systems: A case study of mode-locked lasers,” *Machine Learning: Science and Technology*, vol. 1, no. 4, p. 045013, 2020.
- [111] Q. Yan, Q. Deng, J. Zhang, Y. Zhu, K. Yin, T. Li, D. Wu, and T. Jiang, “Low-latency deep-reinforcement learning algorithm for ultrafast fiber lasers,” *Photonics Research*, vol. 9, no. 8, pp. 1493–1501, 2021.
- [112] E. Kuprikov, A. Kokhanovskiy, K. Serebrennikov, and S. Turitsyn, “Deep reinforcement learning for self-tuning laser source of dissipative solitons,” *Scientific Reports*, vol. 12, no. 1, pp. 1–9, 2022.
- [113] C. G. Atkeson and J. C. Santamaria, “A comparison of direct and model-based reinforcement learning,” in *Proceedings of international conference on robotics and automation*, vol. 4, pp. 3557–3564, IEEE, 1997.
- [114] T. P. Lillicrap, J. J. Hunt, A. Pritzel, N. Heess, T. Erez, Y. Tassa, D. Silver, and D. Wierstra, “Continuous control with deep reinforcement learning,” *arXiv preprint arXiv:1509.02971*, 2015.

- [115] S. Fujimoto, H. Hoof, and D. Meger, “Addressing function approximation error in actor-critic methods,” in *International conference on machine learning*, pp. 1587–1596, PMLR, 2018.
- [116] J. Schulman, F. Wolski, P. Dhariwal, A. Radford, and O. Klimov, “Proximal policy optimization algorithms,” *arXiv preprint arXiv:1707.06347*, 2017.
- [117] D. Silver, G. Lever, N. Heess, T. Degris, D. Wierstra, and M. Riedmiller, “Deterministic policy gradient algorithms,” in *International conference on machine learning*, pp. 387–395, PMLR, 2014.
- [118] V. Mnih, K. Kavukcuoglu, D. Silver, A. Graves, I. Antonoglou, D. Wierstra, and M. Riedmiller, “Playing atari with deep reinforcement learning,” *arXiv preprint arXiv:1312.5602*, 2013.
- [119] H. Van Hasselt, A. Guez, and D. Silver, “Deep reinforcement learning with double q-learning,” in *Proceedings of the AAAI conference on artificial intelligence*, vol. 30, 2016.
- [120] S. Jo, C. Jong, C. Pak, and H. Ri, “Multi-agent deep reinforcement learning-based energy efficient power allocation in downlink mimo-noma systems,” *IET Communications*, vol. 15, no. 12, pp. 1642–1654, 2021.
- [121] R. Stekolshchik, “Noise, overestimation and exploration in deep reinforcement learning,” *arXiv preprint arXiv:2006.14167*, 2020.
- [122] C. C.-Y. Hsu, C. Mendler-Dünner, and M. Hardt, “Revisiting design choices in proximal policy optimization,” *arXiv preprint arXiv:2009.10897*, 2020.
- [123] J. Schulman, P. Moritz, S. Levine, M. Jordan, and P. Abbeel, “High-dimensional continuous control using generalized advantage estimation,” *arXiv preprint arXiv:1506.02438*, 2015.
- [124] V. Mnih, A. P. Badia, M. Mirza, A. Graves, T. Lillicrap, T. Harley, D. Silver, and K. Kavukcuoglu, “Asynchronous methods for deep reinforcement learning,” in *International conference on machine learning*, pp. 1928–1937, PMLR, 2016.
- [125] P. D. Lakshmijayasimha, A. Kaszubowska-Anandarajah, E. P. Martin, P. Landais, and P. M. Anandarajah, “Expansion and phase correlation of a wavelength tunable gain-switched optical frequency comb,” *Optics Express*, vol. 27, no. 12, pp. 16560–16570, 2019.

